Astrocyte layers in the mammalian cerebral cortex revealed by a single-cell in situ transcriptomic map

Omer Ali Bayraktar[1,2,†*], Theresa Bartels[1], Staffan Holmqvist[1], Vitalii Kleshchevnikov[3], Araks Martirosyan[4], Damon Polioudakis[5,6], Lucile Ben Haim[1,2], Adam M.H. Young[7], Mykhailo Y. Batiuk[4], Kirti Prakash[1], Alexander Brown[8], Kenny Roberts[3], Mercedes F. Paredes[2,9], Riki Kawaguchi[11], John H. Stockley[1], Khalida Sabeur[1,2], Sandra M. Chang[1,2], Eric Huang[9,10], Peter Hutchinson[7], Erik M. Ullian[11], Martin Hemberg[3], Giovanni Coppola[5,12], Matthew G. Holt[4], Daniel H. Geschwind[5,6] & David H. Rowitch[1,2,*]

[1]Department of Paediatrics, Wellcome-MRC Cambridge Stem Cell Institute, University of Cambridge, Cambridge, CB20QQ, UK.

[2]Departments of Pediatrics and Neurosurgery, Eli and Edythe Broad Center of Regeneration Medicine and Stem Cell Research, University of California San Francisco, San Francisco, California 94143, USA.

[3]Wellcome Sanger Institute, Hinxton, CB10 1SA, UK

[4]Laboratory of Glia Biology, VIB-KU Leuven Center for Brain and Disease Research, KU Leuven Department of Neuroscience, Leuven, Belgium

Departments of [5]Neurology and Human Genetics, [12]Psychiatry, [6]Center for Autism Research and Treatment, Semel Institute for Neuroscience and Human Behavior, David Geffen School of Medicine, University of California, Los Angeles, Los Angeles, CA 90095, USA.

[7]Division of Academic Neurosurgery, Department of Clinical Neurosciences, University of Cambridge, Cambridge, CB20QQ, UK.

[8]Sainsbury Wellcome Centre, University College London

Departments of [9]Neurology, [10]Pathology, [11]Opthamalogy, University of California San Francisco, San Francisco, California 94143, USA;

[†]Present address: Wellcome Sanger Institute, Hinxton, CB10 1SA, UK

***Authors for correspondence:** Omer Ali Bayraktar, Wellcome Sanger Institute, Hinxton, CB10 1SA, UK; Email: ob5@sanger.ac.uk; David Rowitch, Department of Paediatrics, University of Cambridge, Hills Road, Cambridge, CB2 0QQ; Email: dhr25@medschl.cam.ac.uk

Abstract: While the cerebral cortex is organized into six excitatory neuronal layers, it is unclear whether glial cells show distinct layering. Here, we developed a high-content pipeline, the Large-area Spatial Transcriptomic (LaST) map, which can quantify single-cell gene expression *in situ.* Screening 46 candidate genes for astrocyte diversity across the mouse cortex, we identified superficial, mid, and deep astrocyte identities in gradient layer patterns that were distinct from those of neurons. Astrocyte layer features, established in early postnatal cortex, mostly persisted in adult mouse and human cortex. Single cell RNA sequencing and spatial reconstruction analysis further confirmed the presence of astrocyte layers in the adult cortex. Satb2 and Reeler mutations that shifted neuronal post-mitotic development were sufficient to alter glial layering, indicating an instructive role for neuronal cues. Finally, astrocyte layer patterns diverged between mouse cortical regions. These findings indicate that excitatory neurons and astrocytes are organized into distinct lineage-associated laminae.

Introduction

Cortical structure has classically been described in terms of six excitatory neuronal layers, generated sequentially during early development (*1*). In addition, the cortex is regionally specialized into areas responsible for motor, sensory and cognitive functions (1). Although neurons are known to be a diverse population, astrocytes, which comprise about 50% of brain cells, are generally regarded as functionally homogeneous and interchangeable. Might glia also be regionally specialized to confer added cortical organizational complexity? Gray matter astrocytes generally support central nervous system (CNS) structure, nutrition, regulation of blood flow, the blood-brain barrier, synapse formation and activity (2). While several studies show functional diversity of astrocytes (3-7) with implications for regional neural circuit activity or survival (8), precise molecular features of glial spatial organization underlying cortical architecture remain unclear.

Single-cell spatial transcriptomic approaches can provide unprecedented detail on cellular diversity (9), and have been used to investigate the spatial organization of the mammalian brain (10-12). While some approaches produce highly multiplexed gene expression information, imaging and high-content data analysis restrict their application to relatively small tissue areas. Thus, they leave open the important question of how spatial transcriptomics can be applied to screen large tissue areas, including archival tissues and human organs, in a single-cell and quantitative manner to demonstrate gene expression gradients across regions.

Here we developed a method for automated quantitative high-content screening of *in situ* single-cell gene expression in the mammalian brain. We screened 46 candidate genes for astrocyte spatial organization against known patterns for neurons in the cerebral cortex. Surprisingly, while astrocytes expression patterns showed laminar and area organization such glial layers did not correspond to the six excitatory neuronal layers, indicating higher order complexity of cortical architecture.

Results

Automated pipeline to map single cell cortical gene expression *in situ*. To map single-cell gene expression across large tissue areas at scale, we automated multiplexed branched-DNA single-molecule fluorescent in situ hybridization (RNAScope smFISH, Advanced Cell Diagnostics) with favorable signal-to-noise ratio (13), immunohistochemistry (IHC), fast confocal imaging, cellular segmentation and quantification on standard whole mouse brain cryo-sections (Fig 1A). We used spinning disk confocal microscopy, to image whole tissue sections at high XY and Z resolution, then modified a high-content screening workflow software (Harmony, Perkin Elmer) to quantify RNA transcripts per cell. We manually segmented cells into brain regions based on reference atlases for gene expression analysis (see Extended Methods) to generate quantitative 2D tissue maps showing spatial single cell regulation of gene expression.

LaST map confirms neuron excitatory layering and reveals novel neuronal architecture in mouse postnatal cortex. We first validated our Large area Spatial

Transcriptomic (LaST) pipeline by mapping expression of known cortical layer neuron markers for layers 2-4 (L2-4, *Cux2*), L4 (*Rorb*), L5-6 (*Bcl11b*) and L6 (*Foxp2*) (1) (Fig 1B,C) in the mouse brain. We performed automated six-color imaging of 10 anterior-posterior sections across the entire P14 cortex (Fig 1E, F), totaling 2,216 fields of view and ~300,000 images collected under 25 hours of continuous acquisition. We used machine-learning based texture analysis combined with NeuN IHC (neuronal nuclei and cytoplasm) and DAPI staining to identify single neuron soma on max-z projection images, while also ruling out doublets/triplets (Supplementary Figure 1, Extended Methods). This approach validated that our technique accurately identified known layer-specific single-cell and layer-specific neuronal gene expression patterns (Fig 1C) with robust reproducibility (Supplementary Figure 2).

Having generated a quantitative map of known cortical neuron gene expression, we tested whether we could identify and/or discover neuronal subtypes solely from smFISH data in an unbiased manner. We analysed transcript counts from 46,888 neurons across select broad cortical areas using a modified dimensionality reduction and hierarchical clustering approach (Extended Methods, Sup Table 1). Our analysis identified 10 distinct major clusters based on the expression of the four markers above (Fig 1D) and could robustly detect low expression differences across neurons (Supplementary Figure 3,4,5). These clusters primarily represented layer-enriched neuron populations present across multiple cortical areas (Fig 1C, D, G;, e.g. $Bcl11b^{high}Foxp2^{high}$ cluster #9 in L6). In addition, we captured heterogeneity within cortical layers, exemplified by clusters of $Cux2^{high}Rorb^{neg/low}$ (#1,3-5) and $Cux2^{high}Rorb^{high}$ (#8) within L2-3. We could also accurately distinguish area-specific differences such as $Rorb^{high}Cux2^{high}$ neurons (#6 and

8) enriched in L4 of sensory areas and *Cux2*^{mid}*Bcl11b*^{mid} neurons (#2, likely an interneuron subtype, Supplementary Figure 6, , (14)) in L1-3 and L5 of somatosensory, motor and auditory cortex (full area maps shown in Supplementary Figure 7). Finally, we found a novel population of *Rorb*^{high}*Cux*^{mid}*Bcl11b*^{low} neurons (#7) restricted to L5 of anterior somatosensory, barrel and visual cortex at P14 and P56 (Fig 1C, H; Supplementary Figure 6). To confirm that *Rorb* and *Bcl11b* expression segregates amongst neuronal subtypes in L5, we examined available cortical single cell transcriptome data (15). Consistently, our survey showed that *Rorb* and *Bcl11b* expression segregate amongst molecular subtypes of L5 neurons in the adult visual cortex (Supplementary Figure 6). Taken together, these results demonstrate that LaST map can be used to validate regional qualitative and quantitative predictions about gene expression in mammalian brain and that it can serve as a tool to sensitively identify novel/diversified cell populations *in situ.*

Laminar gene expression patterns are characteristic of cortical gray matter astrocytes. It is generally accepted that astrocytes in the superficial subpia (L1) and deep L6 show white matter astrocyte characteristics (16). We next tested whether gray matter astrocytes in L2-5 are molecularly homogeneous, or alternatively, segment into multiple distinct layers? First, to generate candidate gene lists, we manually dissected the upper (L2-4) and deep (L5-6) layers of the somatosensory cortex from P14 astrocyte reporter *Aldh1L1-GFP* transgenic mice (17) and performed RNA-seq profiling of FACS-purified astrocytes versus whole cortex (Fig 2A). The expression pattern of whole cortical tissue showed that the microdissection accurately captured upper and deep layers. Astrocyte markers were highly enriched in FACS-purified GFP+ cells over GFP-negative cells and

whole cortex tissue as expected; moreover, most neuronal layer markers were not distinctly expressed amongst cortical astrocytes (Supplementary Figure 8).

This analysis identified 159 candidate genes with a differing expression between the upper and deep layer astrocytes (Fig 2B). While most genes showed moderate-layer enrichment, many also showed layer and astrocyte-enriched expression in published cortical transcriptome datasets (Supplementary Figure 9). We next validated layer astrocyte gene expression *in situ*. To distinguish astrocyte-specific gene expression by smFISH, we examined markers for astrocytes (*Aldh1l1, AldoC, Glast*), neurons (*Syt1,* NEUN), oligodendrocytes (*Pdgfra, Plp*), microglia (*Tmem119*) and endothelia (*Tie1*) (17). As shown in Fig 2C-G, while *Glast* mRNA showed low expression in *Pdgfra*+ oligodendrocyte precursors, high *Glast* levels exclusively marked astrocytes. *Glast* mRNA (but not *AldoC* or *Aldh1L1*) filled astrocyte soma and main processes, permitting clear delineation of astrocyte cell borders by image texture analysis.

To avoid double counting, we selected non-overlapping single astrocytes by filtering cells based on size, DAPI (single-nuclei) and *Glast* intensity (Extended Methods, Supplementary Figure 10 and 11). In addition, we filtered astrocytes and their processes that overlap with neuronal soma and non-astrocyte nuclei in z-projection images (Fig 2C, Extended Methods). These measures ensured our smFISH approach counted single cell astrocyte-specific gene expression *in situ* in the context of a large tissue area screen.

To validate candidate layer-associated astrocyte genes *in situ*, we first analyzed the P14 somatosensory barrel cortex. We selected the top 46 genes from RNA-seq that showed the highest differential enrichment between cortical layers and/or astrocyte specificity

(Fig 2H, Sup Table 2). Of these, we confirmed layer enriched expression patterns or rejected genes that showed subtle variations based on quantitative findings *in situ*. For example, 48% (22/46) showed an expression pattern biased –but not restricted-- to upper layers (e.g., *Tnfrsf19, Mfge8*), and 15% (7/46) showed enrichment in all gray matter astrocytes across L2-6 (e.g., *Igfbp2, Kirrel2*). Another third (13%, 6/46) showed expression in astrocytes + neurons and were excluded (e.g., *Ddit4l, B3galt2,* Supplementary Figure 12). In contrast, eight genes clearly distinguished upper versus deep layer astrocytes in the somatosensory cortex (Fig 2H). As shown (Fig 3A-C, Supplementary Figure 13), expression of the BMP antagonist Chordin-like 1 (*Chrdl1*) (18) was expressed in L2-4 astrocytes while Interleukin-33 (*Il-33*) (19) was enriched in L5-6 . In distinction, Sciellin (*Scel*), a component of epithelial cornified envelopes (20), was expressed in mid-cortical (~L4) layers and transcriptional repressors *Id1* and *Id3* occupied deep (L5-6) and marginal (L1) layers (21). These findings show that subsets of cortical gray matter astrocytes show laminar spatial gene expression heterogeneity.

Astrocyte layers diverge from neuronal laminae. To determine whether glial layers matched excitatory neurons we directly compared the spatial expression patterns of the 8 top layer astrocyte markers against layer neuron markers in P14 somatosensory barrel cortex *in situ*. We found that astrocyte layer genes generally fell into three spatial bins comprising superficial, mid and deep laminae. As shown (Fig 3A-D, Supplementary Figure 13), *Chrld1, Scel, Eogt, Spry1, Paqr6* and *Il33* were expressed in patterns that spanned multiple neuronal layers. Astrocyte *Chrdl1* expression peaked in L2-4, with low levels in L1 and L5. *Scel* expression was highest in L4-5, with an upper boundary in mid L2-3. *Il33* expression peaked in L5, with low levels in L4 and L6. Such patterns were not

181 artifacts of astrocyte size or *Glast* expression level differences across layers
182 (Supplementary Figure 14) and were highly reproducible with expression levels similar
183 to that of layer neuron markers (Supplementary Figure 15). The layer astrocyte patterns
184 were also validated with immunohistochemistry (Supplementary Figure 16). Moreover,
185 analysis of the P56 mouse brain indicated persistence of these patterns, except for the
186 mid-layer *Scel* expression into adulthood (Fig 3D). Indeed, we found that the upper layer
187 astrocyte *Chrdl1* expression was conserved in the adult human brain (Fig 3E,
188 Supplementary Figure 17).

189 While we found certain similar features between astrocytes in deep cortical layers and
190 white matter (WM), most cortical astrocyte layer genes were specific to gray matter. L6
191 astrocytes expressed high levels of *Gfap*, *Id1* and *Id3*, similar to astrocytes in subcortical
192 WM and L1-subpia (Supplementary Figure 13) (7). Conversely, *Il33* was enriched in L5-
193 6 gray matter astrocytes but absent from WM, showing that deep layer astrocyte identity
194 is distinct from WM. Together, these findings indicate that astrocytes are organized into
195 multiple layers across the cortical gray matter and that several glial laminae are dissimilar
196 to classic neuronal layers (Fig 6E). Moreover, such patterns are evident from P14, persist
197 until adulthood and are conserved in the human cortex.

198 **Astrocyte layers are observed in unbiased single cell transcriptomic data.** To
199 independently verify astrocyte layers, we examined the molecular heterogeneity of
200 cortical astrocytes in a single-cell RNA-seq (scRNA-seq) study (Fig 4A). The single cell
201 astrocyte transcriptomic database was generated using a modified Smart-Seq2 protocol
202 (23). Unsupervised clustering with the Louvain method identified two major astrocyte

subtypes in the P56 cortex (Fig 4C). These astrocyte clusters, designated AST2 and AST3, were distinguished by the expression of *Unc13c* and *Agt*, respectively (Fig 4C), and were found to be largely intermixed throughout cortical layers (23). To reconcile our results with these findings, we examined the expression pattern of our cardinal layer astrocyte markers in the scRNA-seq data. As shown (Fig 4D), our layer astrocyte markers were expressed in subpopulations of cells in the single astrocyte transcriptome data, but not in a cluster-associated way. These observations suggest that, while layer astrocyte gene expression patterns can be detected in an unbiased transcriptomic study of cortical astrocytes, there might be multiple axes of astrocyte heterogeneity (i.e. laminar and non-laminar) in the cortex.

To determine whether astrocyte layering represents an axis of heterogeneity in the single cell transcriptome data, we then mapped the scRNA-seq data to cortical layers using the smFISH data as a spatial reference (Fig 4B). To infer the cortical layer position of cells profiled in scRNA-seq, we employed a Bayesian model (22) using 16-layer astrocyte markers profiled with LaST map smFISH as a reference. The spatial reconstruction allowed us to assign cells to different layers with high accuracy (Fig 4F, Supplementary Figure 18) and distinguish astrocyte layers in the single cell transcriptome data (Fig 4E). The two cortical astrocyte subtypes identified by unsupervised clustering of scRNA-seq were both located across multiple layers (Fig 4E, Supplementary Figure 19), consistent with the observation that they are spatially intermixed (23). We also found that scRNA-seq clusters derived using the alternative SC3 method showed a similar non-layer specific distribution (Supplementary Figure 19). Taken together, these results suggest that cortical astrocytes show at least two axes of molecular diversity: 1) layer-independent

heterogeneity detected by unsupervised clustering of scRNA-seq data and 2) layer-dependent heterogeneity demonstrated by our smFISH-based approach and the spatial reconstruction of scRNA-seq data.

Spatial reconstruction of single astrocyte transcriptomes identifies new layer astrocyte genes. To expand the repertoire of astrocyte layer markers, we used spatial reconstruction of single cell transcriptomes (22). This analysis yielded 125 genes with layer-associated expression features. Layer-associated astrocyte candidate genes comprised on average 19% percent of transcripts per cell and 8% of expressed genes (Supplementary Figure 18, Kruskal–Wallis FDR-corrected p-value < 0.05); of these, 2/3 were predicted to exhibit upper and deep layer astrocyte expression (similar to *Chrdl1* and *Il33*), while the remaining third of genes exhibited WM-like layer profiles (similar to *Id3*, Fig 4G, Supplementary Figure 18). We validated three of these predictions with smFISH. As shown (Fig 4H-J), the expression of the transcriptional regulator Nuclear Protein 1 (*Nupr1*) peaked in L2-4 astrocytes, while the enzyme Epoxide Hydrolase 2 (*Ephx2*) and the proteolipid Neuronatin (*Nnat*) showed higher expression in deep layer L5/6 astrocytes. Thus, interrogation of scRNA-seq data provides additional insight into the degrees of astrocyte layer heterogeneity in cerebral cortex.

Neuronal specification directly or indirectly determines astrocyte laminar gene expression. During cortical development, neuronal layers are established along a radial glial scaffold prior to astrogenesis (P0-7 (24)). To investigate whether neuronal factors regulate astrocyte layer organization, we first examined mice that lack the chromatin remodeling factor *Satb2*, which is required to specify superficial post-mitotic callosal

neuron identity (25) *Satb2* conditional knockout mice (*Satb2* cKO*, Emx1-cre x Satb2 floxed/floxed)* are deficient in L2-4 neuron gene expression, lack callosal axon projections and ectopically express markers of L5-6 neurons in superficial cortical layers (26,27).

We verified that at P14, L4 neurons (*Rorb, Pamr1*) are absent in *Satb2* cKO while L2-3 neurons show some ectopic deep layer gene expression (*Bcl11b*) (Fig 5A, C, Supplementary Figure 20). As a consequence, we found complete loss of *Scel* expression in astrocytes, while upper layer astrocyte genes *Chrdl1* and *Eogt* were significantly reduced (Fig 5B, D). Deep layer astrocyte genes (*Il33, Id1, Id3*) were unaffected. These findings indicate that post-mitotic L4-specific neuron identity is necessary for the generation of superficial layer astrocyte identity (Fig 5I). Next, to assess deep layer astrocyte identity in relation to neurons, we used *Reeler (Reln)* mice, deficient for secreted Reelin, that show an inversion of radial glial polarity and neuronal layers (28). In *Reln* mice excitatory neurons are specified correctly but fail to migrate to their proper layers, yielding an "inside-out" cortex before birth (29). As expected (30), at P14 the expression pattern of superficial (*Cux2*) and deep laminar markers (*Bcl11b, Foxp2*) were inverted while L4 neurons (*Rorb*) formed aberrant clusters across cortical depth (Fig 5E-G). In addition, we found that superficial and deep astrocyte layers were inverted (Fig 5F-H). Consistent with the L4 neuron phenotype, *Scel*+ astrocytes were aberrantly located across cortical depth. Together, these findings suggest that cortical neuronal cues are involved in regulation of astrocyte layer development (Fig 5I).

Astrocyte layer characteristics vary between cortical areas. Are astrocyte layers distinct or similar between functional cortical areas? To investigate astrocyte arealization,

we quantified patterns of top layer astrocyte markers across the P14 cortex. As shown (Fig. 6), astrocyte layer gene expression varied significantly across dorsoventral and rostrocaudal cortex. *Scel* expression showed enrichment in L4-5 astrocytes in the somatosensory areas but was absent from the medial motor and caudal visual cortex (Fig 6A, B), a pattern that correlates closely with L4 neurons (Fig 6D). In a different pattern, *Chrdl1* showed dorsoventral enrichment in L1-4 astrocytes throughout the cortex (Fig 6C). In contrast, deep layer astrocyte marker expression was enriched in medial and lateral areas across the dorsoventral axis (*Il33, Id3*, Fig 6D, Supplementary Figure 21, 22). Thus, astrocytes show both laminar and area heterogeneity across the cortex. Collectively, our observations on the regional heterogeneity of cortical astrocytes and their induction by neuronal signals show that glial laminae are a fundamental biomarker characteristic of cortical layer and area architecture (Fig 6E, F).

Discussion

Our findings indicate LaSTmap as a robust technique to validate single cell gene expression *in situ* as well as discovery of combinatorial patterns indicative of cell diversity. For example, our findings indicate a novel *Rorb, Bcl11b* L5 neuronal sub-type in visual cortex, as well as molecular diversity of cortical gray matter astrocytes. While a prior study indicated morphological and gene expression differences in gray matter versus white matter/L6 cortical astrocytes (7), a surprising biological finding of our study is that cortical gray matter astrocytes are organized into laminae that are distinct from classic layers of excitatory neurons. Moreover, our study identified distinct gray matter astrocyte sub-types within gray matter L2-5. Single-cell quantification of astrocyte layer genes uniquely showed peaks and troughs of expression across the superficial-to-deep cortex, as well as differences across functionally distinct cortical areas. As prior studies show that region-restricted astrocyte mRNA and protein expression are predictors of functions tailored to support of local neural circuits (8,31,32), astrocyte laminar genes indicate potential additional localized functions. Indeed, a recent study showed that expression of *Chrdl1* in upper layer astrocytes is essential for local synapse regulation and regulation of developmental plasticity (33).

By introducing an *in silico* spatial reconstruction approach, we identified and validated further markers of layer-restricted astrocytes *in situ.* This indicates that identification of cell type- and region-specific markers by LaSTmap can used to interrogate other datasets for insights into diversified function, which could play into sophisticated layer-associated neural circuit activity (34). Interestingly, in a companion

311 analysis, genes from cortical astrocytes self-organized into two classes with largely
312 excitatory or inhibitory synapse character across layers (23). Together, these findings
313 suggest that astrocyte laminae include a further axis of heterogeneity in terms of
314 interactions at the synapse level in excitatory or inhibitory circuits.

315 International collaboratives such as the Human Cell Atlas and BRAIN initiative
316 have generated large repositories of gene expression data, and a logical next step is to
317 map back such expression patterns *in situ* within developing tissues and/or mature
318 organs. However, spatial transcriptomic analysis in human tissue presents a particular
319 scaling challenge. LaSTmap provides a pipeline to map quantitative gene expression in
320 single cells across large mouse and human tissue areas. It uses commercially available
321 probes and does not require special tissue preparation or bespoke imaging equipment.
322 LaSTmap showed reproducibility across multiple tissue samples/sections and should be
323 adaptable for a range of other tissues to obtain regional/qualitative and
324 cellular/quantitative information from ISH reintegrated into 2D tissue maps. Here we
325 focused on image acquisition from sections representing the mouse cerebral cortex and
326 we show that use of LaSTmap is feasible in human cortex for gene expression analysis at
327 the single cell level. Future elaboration with tissue warp integration would enable *in*
328 *silico* 3D map construction (35).

329 Analysis of cortical lamination mutants suggested that neuronal cues are required,
330 directly or indirectly, to establish astrocyte laminae, particularly in L4 where neurons and
331 mid-layer astrocyte layers do match most closely. While results in *Reeler* mice are
332 consistent with astrocyte layering following that of excitatory neuronal layering, we

cannot rule out that a cortical ‘pre-pattern’ instructs astrocyte precursors to respond to neuronal signals or other mediator cells involved in astrocyte specification. Indeed, astrocyte-encoded gradient patterns are typical of cells that have undergone polarization in response to a morphogen, and upstream regulation of this process is a subject for further study.

Together, our findings indicate the diversification of astrocytes in layer patterns that diverge from excitatory neurons, indicating a composite “neuroglial” cortical architecture with higher order complexity. Our study has revealed markers for astrocyte cortical layers that could provide insight into specialized functions in development and/or disease (36).

Author Contributions

O.A.B. and D.H.R. conceived the study. O.A.B. planned the experiments. O.A.B., T.B. and S.H. performed histology and imaging experiments. O.A.B. performed the image analysis. K.P. and J.S. contributed to the histology and imaging pipeline. D.P. and O.A.B. analyzed neuron gene expression data to identify subtypes. A.B. wrote the slideSegmenter software. A.M.H.Y. and M.F.P. provided human tissue. O.A.B. and L.B.H. performed layer astrocyte purification. O.A.B. and R.K. analyzed RNASeq data. A.M., M.B. and M.G.H. generated the astrocyte scRNA-seq data. V.K. and M.H. analyzed the scRNA-seq data and performed spatial reconstruction analysis. K.S. and S.M. supported mouse work and genotyping. O.A.B. and D.H.R. wrote the manuscript with feedback from all authors.

Acknowledgments

We are grateful to Ben Barres and Sarah Teichmann for helpful discussions and comments. We are grateful to Barry Lynch and Xiao-Jun Ma for advice on RNAScope, as well as Richard Sawkins and James Hutt for technical support on imaging. We are also grateful to Eric Olson (SUNY Upstate University) for providing *Reeler* mice and Ralph Marcucio (UCSF) for providing the *Satb2-flox* mice.

Fellowships:

The authors were supported by the Life Sciences Research Fellowship and the Howard Hughes Medical Institute (O.A.B.), the Wellcome Trust (T.B.), NIHR Academic Clinical

Fellowship and a Wellcome Trust PhD for Clinicians Fellowship (A.M.H.Y.) and Stichting Alzheiemer Onderzoek (A.M.).

Grants:

The study was supported by the Paul G. Allen Foundation Distinguished Investigator Program (E.M.U. and D.H.R.), the Dr. Miriam and Sheldon G. Adelson Medical Research Foundation (D.H.R., D.G. and G. C.), BRAIN initiative (1U01 MH105991 to D.G.) and National Institute of Health (1R01 MH109912 to D.G.; P01NS08351 to D.H.R.), National Institute of Health Research and the European Union Seventh Framework (to P.H.), NINDS Informatics Center for Neurogenetics and Neurogenomics (P30 NS062691 to G.C.), Wellcome Trust core support (M.H., O.A.B.), European Research Council (281961 to M.G.H.), Fonds Wetenschappelijk Onderzoek (G066715N and 1523014N to M.G.H.), Stichting Alzheimer Onderzoek (S#16025 to M.G.H.) and VIB Institutional Support and Tech Watch funding (to M.G.H.), Howard Hughes Medical Institute and the Wellcome Trust (to D.H.R.).

Competing financial interests

The authors declare no competing financial interests.

References

1. Molyneaux BJ, Arlotta P, Menezes JRL, Macklis JD. Neuronal subtype specification in the cerebral cortex. Nat Rev Neurosci. 2007 Jun;8(6):427–37.

2. Freeman MR, Rowitch DH. Evolving concepts of gliogenesis: a look way back and ahead to the next 25 years. Neuron. 2013 Oct 30;80(3):613–23. PMCID: PMC5221505

3. Doyle JP, Dougherty JD, Heiman M, Schmidt EF, Stevens TR, Ma G, et al. Application of a Translational Profiling Approach for the Comparative Analysis of CNS Cell Types. Cell. 2008 Nov;135(4):749–62. PMCID: PMC2763427

4. Chai H, Diaz-Castro B, Shigetomi E, Monte E, Octeau JC, Yu X, et al. Neural Circuit-Specialized Astrocytes: Transcriptomic, Proteomic, Morphological, and Functional Evidence. Neuron. 2017 Jul.

5. John Lin C-C, Yu K, Hatcher A, Huang T-W, Lee HK, Carlson J, et al. Identification of diverse astrocyte populations and their malignant analogs. Nat Neurosci. 2017 Feb 6.

6. Boisvert MM, Erikson GA, Shokhirev MN, Allen NJ. The Aging Astrocyte Transcriptome from Multiple Regions of the Mouse Brain. Cell Rep. 2018 Jan 2;22(1):269–85. PMCID: PMC5783200

7. Lanjakornsiripan D, Pior B-J, Kawaguchi D, Furutachi S, Tahara T, Katsuyama Y, et al. Layer-specific morphological and molecular differences in neocortical astrocytes and their dependence on neuronal layers. Nat Commun. Nature Publishing Group; 2018 Apr 24;9(1):1623. PMCID: PMC5915416

8. Molofsky AV, Kelley KW, Tsai H-H, Redmond SA, Chang SM, Madireddy L, et al. Astrocyte-encoded positional cues maintain sensorimotor circuit integrity. Nature. 2014 May 8;509(7499):189–94. PMCID: PMC4057936

9. Lein E, Borm LE, Linnarsson S. The promise of spatial transcriptomics for neuroscience in the era of molecular cell typing. Science. American Association for the Advancement of Science; 2017 Oct 6;358(6359):64–9.

10. Moffitt JR, Hao J, Bambah-Mukku D, Lu T, Dulac C, Zhuang X. High-performance multiplexed fluorescence in situ hybridization in culture and tissue with matrix imprinting and clearing. Proc Natl Acad Sci USA. National Acad Sciences; 2016 Dec 13;113(50):14456–61. PMCID: PMC5167177

11. Shah S, Lubeck E, Zhou W, Cai L. In Situ Transcription Profiling of Single Cells Reveals Spatial Organization of Cells in the Mouse Hippocampus. Neuron. 2016 Oct 19;92(2):342–57. PMCID: PMC5087994

12. Wang X, Allen WE, Wright MA, Sylwestrak EL, Samusik N, Vesuna S, et al. Three-dimensional intact-tissue sequencing of single-cell transcriptional states. Science. American Association for the Advancement of Science; 2018 Jun 21;:eaat5691.

13. Battich N, Stoeger T, Pelkmans L. Image-based transcriptomics in thousands of single human cells at single-molecule resolution. Nat Methods. 2013 Oct 6;10(11):1127–33.

14. Nikouei K, Muñoz-Manchado AB, Hjerling-Leffler J. BCL11B/CTIP2 is highly expressed in GABAergic interneurons of the mouse somatosensory cortex. J. Chem. Neuroanat. 2016 Jan;71:1–5.

15. Tasic B, Menon V, Nguyen TN, Kim TK, Jarsky T, Yao Z, et al. Adult mouse cortical cell taxonomy revealed by single cell transcriptomics. Nat Neurosci. 2016 Feb;19(2):335–46. PMCID: PMC4985242

16. Sosunov AA, Wu X, Tsankova NM, Guilfoyle E, McKhann GM, Goldman JE. Phenotypic heterogeneity and plasticity of isocortical and hippocampal astrocytes in the human brain. J Neurosci. 2014 Feb 5;34(6):2285–98. PMCID: PMC3913872

17. Cahoy JD, Emery B, Kaushal A, Foo LC, Zamanian JL, Christopherson KS, et al. A transcriptome database for astrocytes, neurons, and oligodendrocytes: a new resource for understanding brain development and function. J Neurosci. 2008 Jan 2;28(1):264–78.

18. Nakayama N, Han CE, Scully S, Nishinakamura R, He C, Zeni L, et al. A novel chordin-like protein inhibitor for bone morphogenetic proteins expressed preferentially in mesenchymal cell lineages. Dev Biol. 2001 Apr 15;232(2):372–87.

19. Vainchtein ID, Chin G, Cho FS, Kelley KW, Miller JG, Chien EC, et al. Astrocyte-derived interleukin-33 promotes microglial synapse engulfment and neural circuit development. Science. American Association for the Advancement of Science; 2018 Feb 1;:eaal3589. PMCID: PMC6070131

20. Champliaud MF, Baden HP, Koch M, Jin W, Burgeson RE, Viel A. Gene characterization of sciellin (SCEL) and protein localization in vertebrate epithelia displaying barrier properties. Genomics. 2000 Dec 1;70(2):264–8.

21. Ruzinova MB, Benezra R. Id proteins in development, cell cycle and cancer. Trends in Cell Biology. 2003 Aug;13(8):410–8.

22. Halpern KB, Shenhav R, Matcovitch-Natan O, Tóth B, Lemze D, Golan M, et al. Single-cell spatial reconstruction reveals global division of labour in the mammalian liver. Nature. 2017 Feb 6. PMCID: PMC5321580

23. Batiuk MY, Martirosyan A, Voet T, Ponting CP, Belgard TG, Holt MG. Molecularly distinct astrocyte subpopulations spatially pattern the adult mouse brain. bioRxiv. Cold Spring Harbor Laboratory; 2018 May 10;:317503.

24. Ge W-P, Miyawaki A, Gage FH, Jan Y-N, Jan LY. Local generation of glia is a major astrocyte source in postnatal cortex. Nature. 2012 Apr 19;484(7394):376–80.

25. Alcamo EA, Chirivella L, Dautzenberg M, Dobreva G, Fariñas I, Grosschedl R, et al. Satb2 Regulates Callosal Projection Neuron Identity in the Developing Cerebral Cortex. Neuron. 2008 Feb;57(3):364–77.

26. McKenna WL, Ortiz-Londono CF, Mathew TK, Hoang K, Katzman S, Chen B. Mutual regulation between Satb2 and Fezf2 promotes subcerebral projection neuron identity in the developing cerebral cortex. Proc Natl Acad Sci USA. National Acad Sciences; 2015 Sep 15;112(37):11702–7. PMCID: PMC4577201

27. Leone DP, Heavner WE, Ferenczi EA, Dobreva G, Huguenard JR, Grosschedl R, et al. Satb2 Regulates the Differentiation of Both Callosal and Subcerebral Projection Neurons in the Developing Cerebral Cortex. Cereb. Cortex. 2015 Oct;25(10):3406–19. PMCID: PMC4585495

28. Hartfuss E. Reelin signaling directly affects radial glia morphology and biochemical maturation. DEVELOPMENT- …. 2003 Oct 1;130(19):4597–609.

29. Kwan KY, Sestan N, Anton ES. Transcriptional co-regulation of neuronal migration and laminar identity in the neocortex. DEVELOPMENT- …. 2012 May;139(9):1535–46. PMCID: PMC3317962

30. Boyle MP, Bernard A, Thompson CL, Ng L, Boe A, Mortrud M, et al. Cell-type-specific consequences of Reelin deficiency in the mouse neocortex, hippocampus, and amygdala. J Comp Neurol. Wiley Subscription Services, Inc., A Wiley Company; 2011 Aug 1;519(11):2061–89.

31. Cui Y, Yang Y, Ni Z, Dong Y, Cai G, Foncelle A, et al. Astroglial Kir4.1 in the lateral habenula drives neuronal bursts in depression. Nature. Nature Publishing Group; 2018 Feb 14;554(7692):323–7.

32. Kelley KW, Ben Haim L, Schirmer L, Tyzack GE, Tolman M, Miller JG, et al. Kir4.1-Dependent Astrocyte-Fast Motor Neuron Interactions Are Required for Peak Strength. Neuron. 2018 Apr 18;98(2):306–7. PMCID: PMC5919779

33. Blanco-Suarez E, Liu T-F, Kopelevich A, Allen NJ. Astrocyte-Secreted Chordin-like 1 Drives Synapse Maturation and Limits Plasticity by Increasing Synaptic GluA2 AMPA Receptors. Neuron. 2018 Dec 5;100(5):1116–1132.e13.

34. Marshel JH, Kim YS, Machado TA, Quirin S, Benson B, Kadmon J, et al. Cortical layer–specific critical dynamics triggering perception. Science. American Association for the Advancement of Science; 2019 Jul 18;:eaaw5202.

35. Karreman MA, Mercier L, Schieber NL, Solecki G, Allio G, Winkler F, et al. Fast and precise targeting of single tumor cells in vivo by multimodal correlative microscopy. J Cell Sci. The Company of Biologists Ltd; 2016 Jan 15;129(2):444–56. PMCID: PMC4732291

36. Velmeshev D, Schirmer L, Jung D, Haeussler M, Perez Y, Mayer S, et al. Single-cell genomics identifies cell type-specific molecular changes in autism. Science. American Association for the Advancement of Science; 2019 May 17;364(6441):685–9.

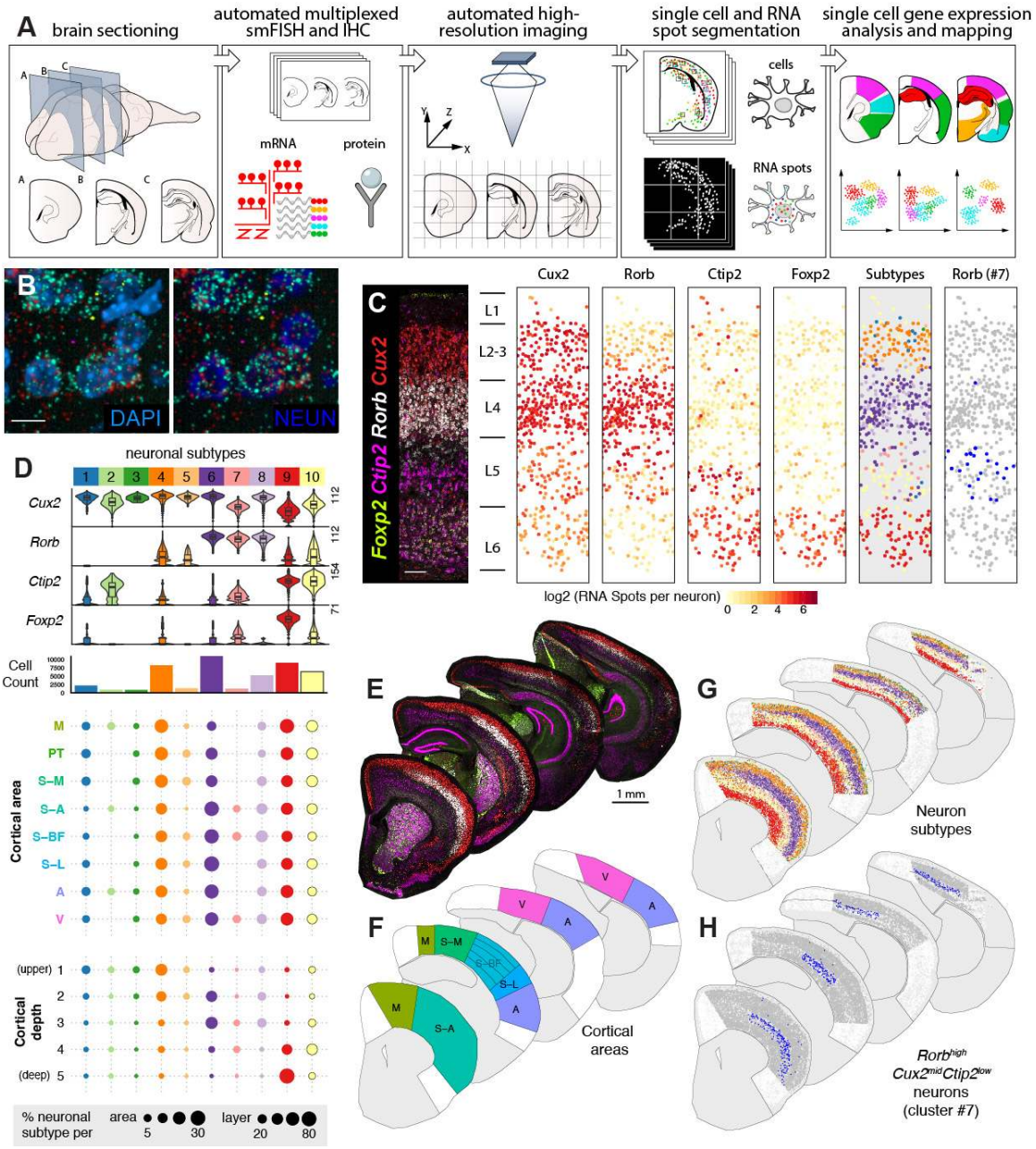

Figure 1: LaST map pipeline for mapping cortical neuronal subtypes *in situ.*

A) Design of automated spatial transcriptomic pipeline.

B) High resolution imaging of large tissue areas. Shown are 40X z-projection images of *Rorb*$^{+}$ L4 neurons in the P14 mouse barrel cortex.

C) Automated mapping of layer neuron marker expression and layer neuron subtypes in the mouse barrel cortex. Automatically identified single neurons are plotted as solid circles and colored according to expression (middle panels) or subtype classification (right panels).

D) Identification of neuronal subtypes based on unbiased classification of single cell level smFISH data. tSNE and hierarchical clustering of 46,888 cortical neurons yielded 10

subpopulations. (Top) Violin plots show single cell expression profiles of clusters, highest RNA spot count per cell are shown on the left. (Middle) Histograms showing total number of cells per cluster. (Bottom) Spatial distribution of clusters across cortical areas and five normalized cortical depth bins, shown as percentage of total neurons in given area/depth bin (bottom).
E-H) Single cell mapping of cortical neuron subtypes: (E) Low magnification images of P14 hemisections from four different anatomical levels, (F) broad cortical areas included in the analysis, (G) maps of 10 major neuronal populations, and (H) spatial distribution of area-restricted L5 *Rorb*^{high}*Cux2*^{mid}*Bcl11b*^{low} neurons.
n = 1 mouse, 10 tissue sections independently imaged. Scalebars: (B) 10 μm, (C) 100 μm, (E) 1 mm.
Abbreviations: M, motor, S-A, anterior- somatosensory, S-M, medial-somatosensory, S-BF, somatosensory barrel, S-L, somatosensory-lateral, PT, parietal, A, auditory, V, visual.

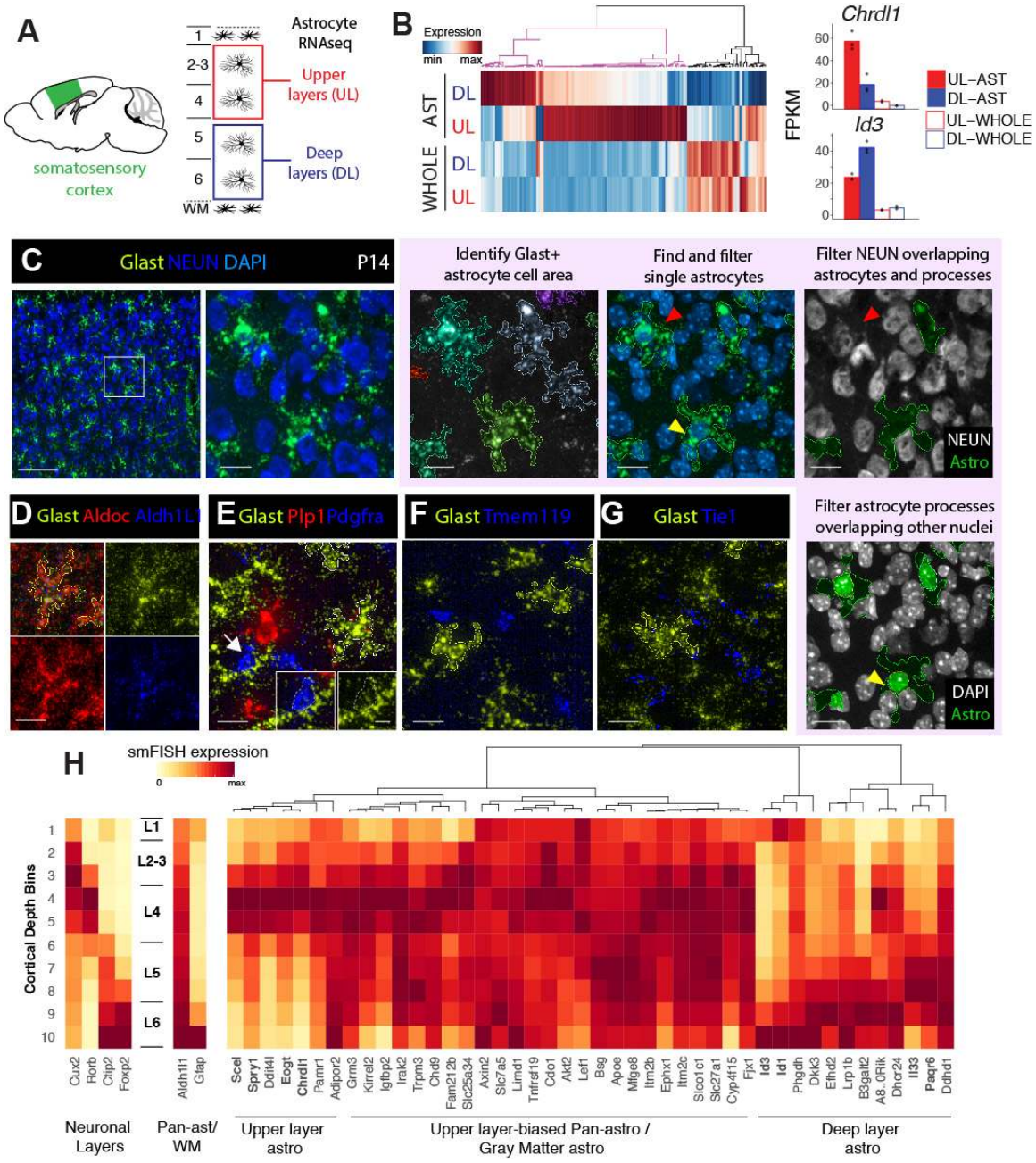

Figure 2: Novel layer expression differences amongst cortical gray matter astrocytes revealed via RNAseq and LaSTmap.

A) Diagram showing somatosensory cortical areas and layers used for laminar gray matter astrocyte RNAseq expression profiling.

B) Novel molecular heterogeneity of layer astrocytes identified by RNAseq. 159 differentially expressed genes between upper and deep layer gray matter astrocytes (FDR<0.05 and expression threshold of FPKM>5) were detected. Bar plots show mean expression (n=3 mice for astrocytes, 2 mice for whole cortex).

C) Identification of astrocyte gene expression with *Glast (Slc1a3)* smFISH. The astrocyte cell area is segmented from the *Glast* signal and nuclei are segmented from DAPI. Single

astrocytes are selected using morphological and intensity filters, overlapping neurons and non-astrocyte nuclei are excluded.
D-G) *Glast* is a specific marker of astrocytes. Solid outlines indicate the cell areas of identified single astrocytes.
H) Screening candidate layer astrocyte genes with LaSTmap identifies laminar expression patterns *in situ*. Tile heatmaps show average single cell gene expression binned across cortical depth in the P14 somatosensory cortex (n =2 pooled biological replicates across multiple tissue sections). Upper and deep layer genes with astrocyte-specific expression are marked in bold. $n = 2$ mice independently assayed, 3 tissue sections imaged per replicate.
Scalebars: (C, left panel) 100 μm, (C, other panels) 25 μm, (D-G) 25 μm, (E, inset) 10 μm.

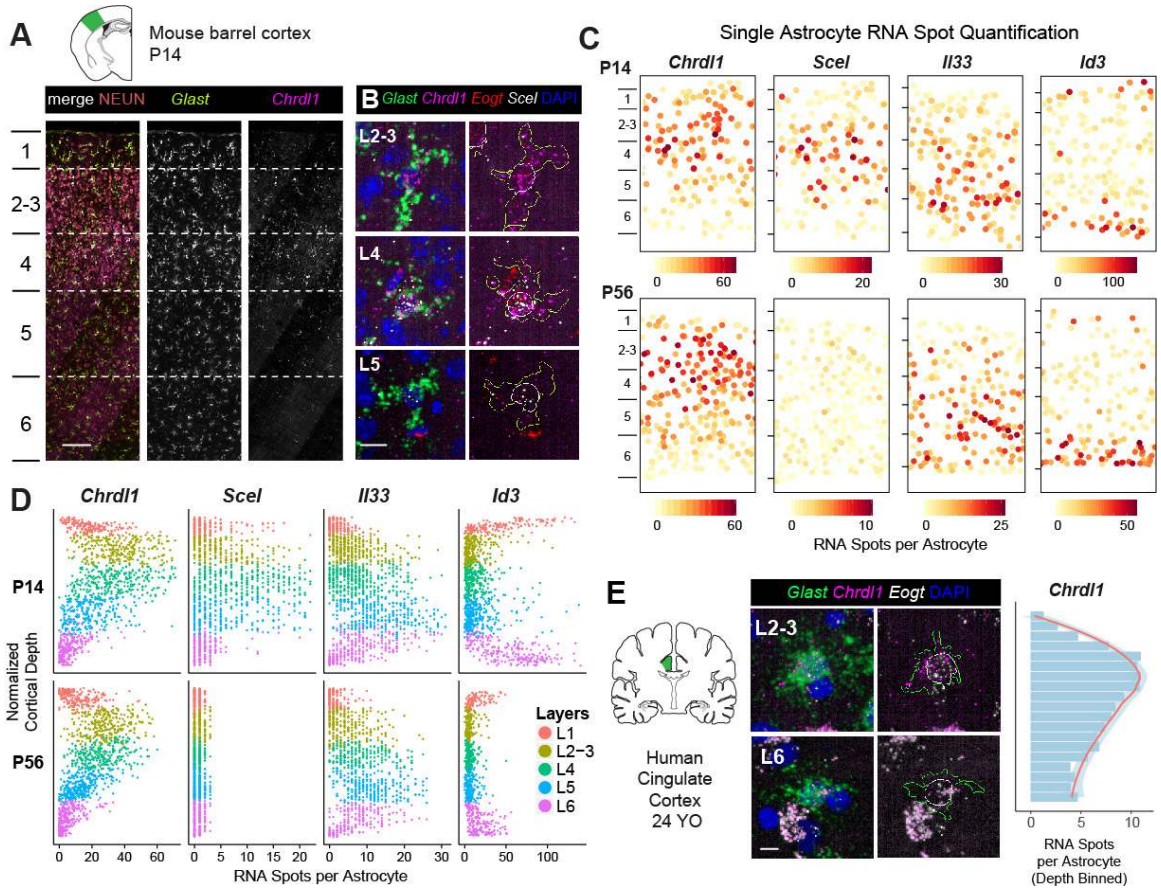

Figure 3: Astrocytes show broad expression gradients across cortical depth and diverge from neuronal layers.

A-B) Upper layer astrocyte enrichment of *Chrdl1, Scel and Eogt.* Images show the mouse barrel cortex at P14 (A) and close-ups of astrocytes across layers (B). Astrocyte cell areas are marked with yellow outlines and nuclei are marked with white outlines.

C) Astrocytes are organized into superficial, mid and deep layers across the cortical gray matter. Single astrocyte expression maps in the barrel cortex at P14 (top panels) and P56 (bottom panels). Astrocytes are plotted as solid circles and colored quantitively for RNA spot counts per gene per cell.

D) Single astrocyte quantification of layer astrocyte markers across cortical depth in the barrel cortex at P14 and P56.

E) Upper layer astrocyte enrichment of *Chrdl1* expression in the adult human cingulate cortex. Quantification of depth binned average single astrocyte expression shown on the right.

n=1 mouse per timepoint, 3 tissue sections imaged independently per gene panel (A-D) and 3 human brains independently assayed, 1-2 sections imaged per case (E).

Scalebars: (A) 100 µm, (B, E) 10 µm.

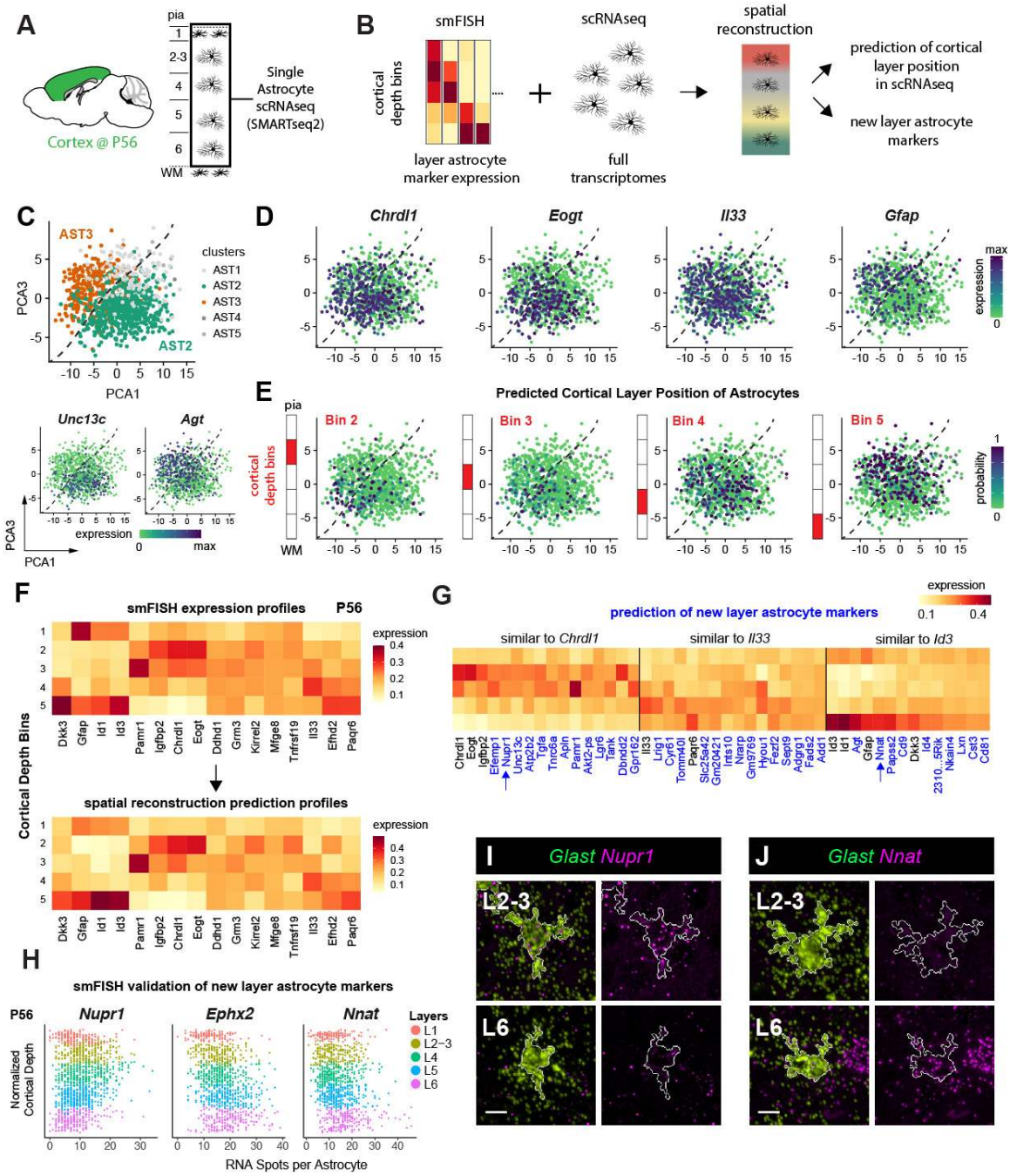

Figure 4: Spatial reconstruction of astrocyte layers from single cell transcriptome data.

A-B) Diagrams showing cortical areas and layers used for single astrocyte RNAseq expression profiling (A) and strategy for spatial gene expression reconstruction (B). **C)** Astrocyte clusters in scRNA-seq data visualized using PCA plots (PC1: 3% PC2: 0.77%. of variance). Dashed lines indicate the border between the major clusters AST2 and AST3 (colors, top). Bottom plots show the expression of cluster markers (log2 Smart-seq2 read counts). $n = 2$ independent experiments.

D) Astrocyte layer markers express in subpopulations of astrocytes in scRNA-seq data but not in a cluster-specific manner. PCA plots are shown.
E) Predicted astrocyte layering across scRNA-seq data as a new axis of heterogeneity. PCA plots (X-axis is PC 1, Y-axis is PC 3) indicate the probability of cell assignment (color) to the cortical depth bins as diagrammed.
F) The smFISH reference of 16 layer astrocyte markers used for the reconstruction (top) and the predicted output of the reconstruction(bottom). Expression scaled to sum to 1 across bins (Y-axis).
G) New candidate layer astrocyte genes predicted by the spatial reconstruction model. The expression pattern of top 10 new layer astrocyte genes (X-axis) that are most similar to *Chrdl1*, *Il33* and *Id3* are shown. Expression scaled to sum to 1 across bins (Y-axis).
H-J) Validation of three new candidate layer astrocyte genes using LaSTmap smFISH. Single astrocyte quantification across cortical depth in the barrel cortex at P56 (n=3 pooled tissue sections from one replicate per timepoint) (H). Close-up images of astrocytes. White outlines mark astrocyte cell areas (I,J). *n*=2 mice independently assayed, 3 sections imaged.

Scalebars: (I,J) 10 μm.

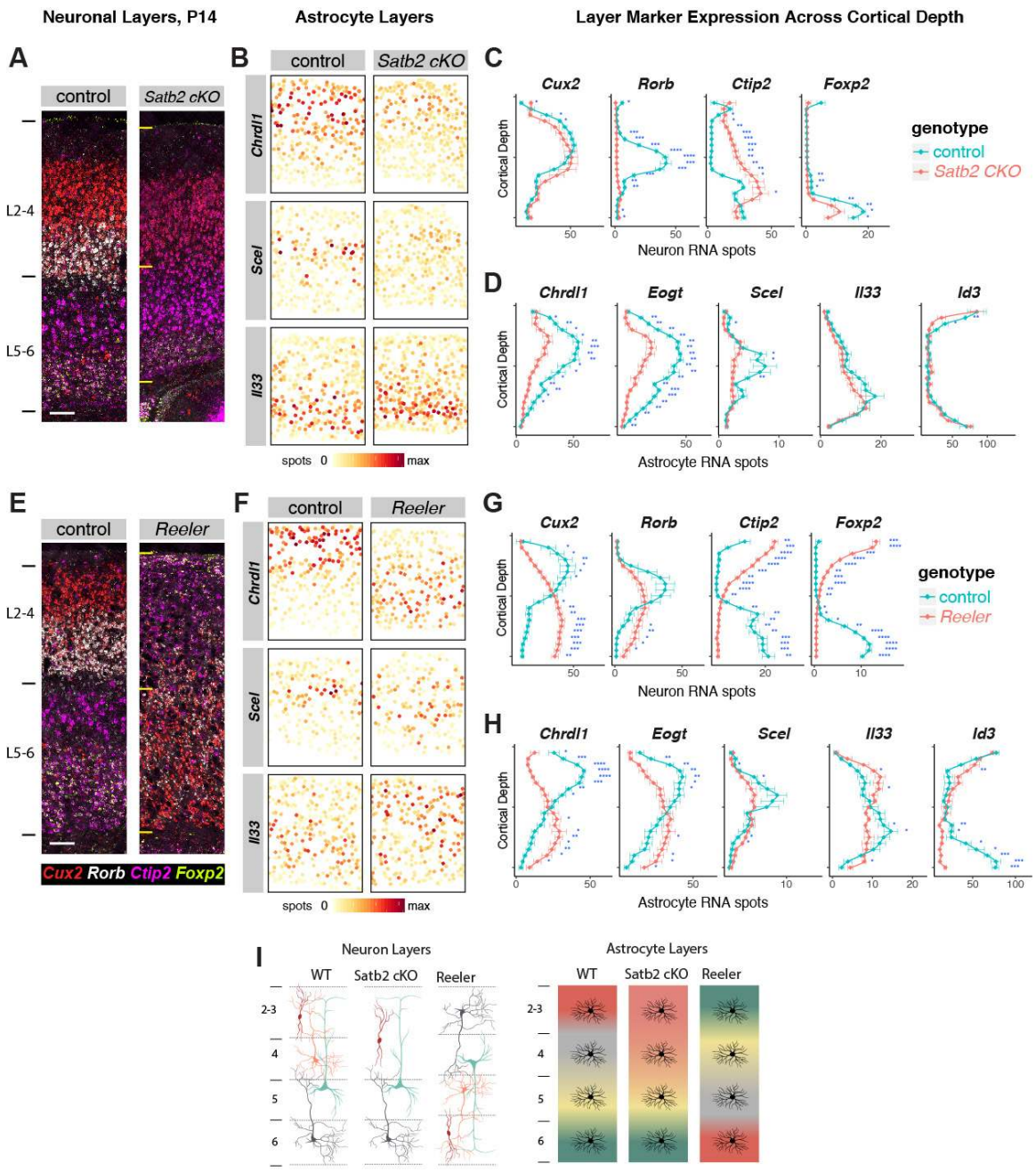

Figure 5: Evidence that post-mitotic neuronal cues establish astrocyte layer identities.

A-D) *Satb2* cKO mice show defects in upper layer neuron and astrocyte identity.

A) Images showing aberrant upper neuronal layers in the *Satb2* cKO barrel cortex at P14.

B) Single astrocyte maps of layer astrocyte marker gene expression.

C-D) Quantification of cortical depth binned layer neuronal (C) and astrocyte (D) marker expression in cKO vs control.

E-H) *Reeler* mice show inversion of neuronal and astrocyte layers.

E) Images showing neuronal layer inversion in the *Reln*-/- barrel cortex at P14.

F) Single astrocyte maps of layer astrocyte marker gene expression.

G-H) Quantification of cortical depth binned layer neuronal (G) and astrocyte (H) marker expression in cKO vs control.
I) Diagrams depicting layer neuron and astrocyte changes in *Satb2* cKO and *Reln-/-* mice.
n= 3 mice per genotype independently assayed, 5 tissue sections from each replicate imaged.
Scalebars: 100 μm. All data represent mean ± s.d. : Two-tailed Student's t-tests were used with *P < 0.05,**P < 0.01, ***P < 0.001.

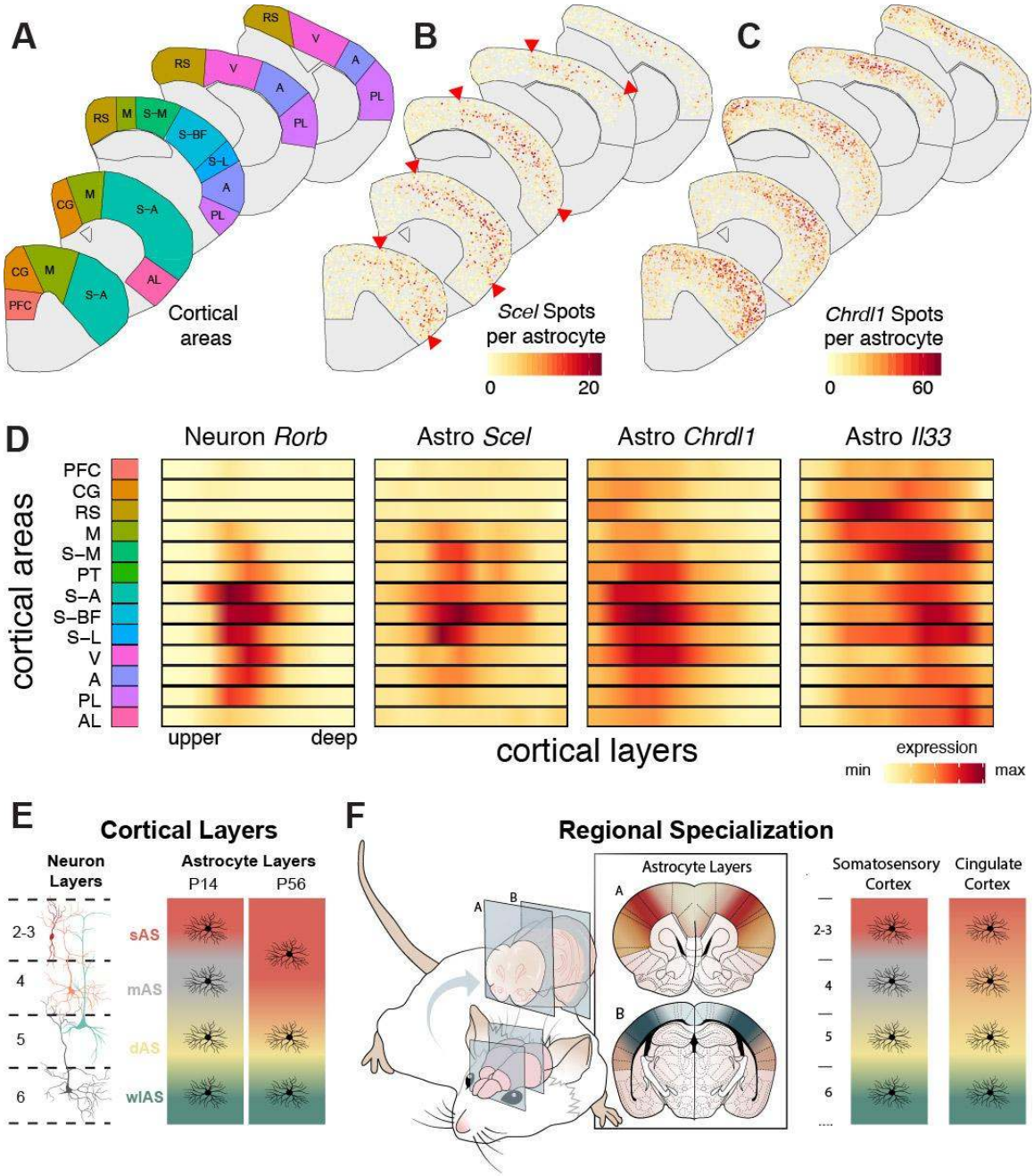

Figure 6: ***Astrocyte arealization across the cortex.***

A-C) Single cell mapping of astrocyte gene expression across cortical areas. Maps show the (A) P14 cortical areas used in the analysis, (B) single astrocyte expression of *Scel* and (C) *Chrdl1* across the dorsoventral and rostrocaudal extent of the cortex. Astrocytes are plotted as solid circles and colored quantitively for RNA spot counts per gene per cell. Arrowheads indicate the restriction of *Scel* expression to sensory areas. Abbreviations as in Fig 1.

D) Astrocyte layers are distinct across cortical areas. Smoothened tile plots showing the quantification of neuronal *Rorb* expression and astrocyte expression of *Scel, Chrdl* and *Il33* across the cortical areas and layers

E) Diagrams showing the divergent layer heterogeneity of astrocytes. Our study identifies superficial (sAS), mid (mAS) and deep (dAS) layer astrocyte subtypes through cortical gray matter in the postnatal cortex and confirms white matter like (wlAS) properties of L6 astrocytes.
F) 3D model showing astrocyte area and layer heterogeneity. Astrocyte layering is regionally specialized across the dorsoventral and rostrocaudal extent of the cortex. $n = 1$ mouse, 10 tissue sections independently imaged.

Supplementary Methods

Mice

All mouse strains were maintained at the University of California, San Francisco (UCSF) specific pathogen-free animal facility and all animal protocols were approved by and in accordance with the guidelines established by the Institutional Animal Care and Use Committee and Laboratory Animal Resource Center. The day of birth was designated as Postnatal day 0 (P0).

Unless otherwise started, wild-type Swiss Webster mice were used for histology and spatial transcriptomics. *Aldh1l1-GFP* transgenic mice were generated by the GENSAT project (37). *Emx1-cre* mice were obtained from The Jackson Laboratory (JAX #005628) (38). Satb2-flox mice were a gift from Dr. Ralph Marcucio at UCSF (27). Conditional knockouts were generated by breeding *Emx1-cre/+; Satb2-flox/+* with *Satb2-flox/flox* mice to obtain mutants (*cre/+; flox/flox*) and littermate controls (*cre/+;flox/+*). *Reeler* (*Reln/Reln*) mice were a gift from Dr. Eric Olson at SUNY Upstate University (B6C3Fe a/a-Reln; JAX). Reln/+ mice were used as littermate controls. All mice were maintained on a mixed background.

Mouse tissue preparation

Mice were transcardially perfused at P14 or P56 with ice-cold phosphate buffer saline (PBS) and 4% paraformaldehyde (PFA) in 1X PBS. Brains were dissected and post-fixed in 4% PFA for 24 hours at 4^{o}C. Post-fixed brains were cryo-protected in 30% sucrose for 48 hr at 4^{o}C and embedded in optimal cutting temperature compound (Tissue-Tek). Cryosections (16 microns) were collected on superfrost slides (VWR) using a cryostat (CM3050S, Leica) and stored at -80^{o}C.

Human tissue

Human brain tissue was obtained with informed consent under protocol 16/LO/2168 approved by the NHS Health Research Authority at the Addenbrookes Hospital. Adult brain tissue biopsies were taken from the site of neurosurgery resection for the original clinical indication. For the purposes on this study samples were taken from peri-contusional areas in traumatic brain injury (frontal cortex), lobectomy in epilepsy surgery (temporal cortex) and peri-tumoural tissue (temporal cortex).

Tissue specimens were collected in Addenbrookes Hospital and transferred to a CL2 facility where it was processed. Tissue was dissected and fixed in 4% PFA for 48-72 hours. Once fixed, samples were placed in 20% Sucrose for cryoprotection for 24-48 hours and mounted in OCT, stored at -80C.

Additional human brain tissue was collected in a de-identified manner with previous patient consent in strict observance of the legal and institutional ethical regulations of the University of California, San Francisco (UCSF) Committee on Human Research. Protocols were approved by the Human Gamete, Embryo and Stem Cell Research Committee (Institutional Review Board) at UCSF. For this study, one post-mortem sample was taken from the superior frontal gyrus and processed as above. Human brain blocks were cryosectioned to 16 microns.

smFISH assay design and probes

Mouse and human tissue smFISH was performed using the RNAScope LS Multiplex Assay (Advanced Cell Diagnostics, ACD) (39). In this assay, the smFISH signal-to-noise ratio (SNR) is amplified by branched DNA complexes formed on target transcripts and tyramide signal amplification (TSA)-based labeling. Target RNAs are initially hybridized to a series of single-stranded DNA "z-probes". Each z-probe is composed of (**1**) a 18-25 nucleotide region complementary to the target RNA, (**2**) a spacer sequence, and (**3**) a 14 nucleotide tail region. These probes are tagged by branched DNA-amplification trees: pairs of z-probes are hybridized to oligo-preamplifiers, across their bridged tail sequences, which are then tagged by 20 oligo-amplifiers (Fig 1 A). Each oligo-amplifier is labeled with 20 Horse Radish Peroxidase (HRP) enzyme molecules. In general, a 1 kilobase region on the target transcript is hybridized by 20 z-probe pairs in tandem, which can yield up to 8000 HRP labels per each target. The fluorescent smFISH signal is consequently generated by the addition of tyramide-conjugated fluorophores. Tyramide is enzymatically converted into a highly oxidized intermediate by HRP that covalently binds to the proteins at or near the HRP label, depositing a large number of fluorophores for probe detection (40). The combination of branched DNA and TSA-amplification significantly boosts the sensitivity and SNR of the RNAScope assay, allowing fast confocal imaging of large tissue areas with short exposure times (see imaging).

Multiplexed detection: To achieve 4-plex transcript detection with RNAScope, target z-probes are assigned to one of four different channels (C1-C4) that contain distinct tail-sequences. Tissue samples are hybridized to the mixture of C1-C4 probes, followed by generation of channel-specific amplification trees. Finally, probes are sequentially developed with TSA through incubation cycles of channel-specific HRP labels, tyramide-conjugated fluorescent dyes and chemical enzymatic quenchers.

Probe information: All of the RNAscope probes used in this study and relevant information including target sequences are listed in Supplementary Table 3. Further information is readily available from the vendor (https://acdbio.com/catalog-probes). To assess the background signal from the assay, target probes against the bacterial *DapB* mRNA were used as negative controls. Target probes against mouse and human housekeeping genes were used as positive controls. In the mouse cortical astrocyte expression screen, the *Glast* probe was always assigned to C4 and multiplexed with other probes in C1-C3 channels. With human tissue, the *Glast* probe was assigned to C3 and multiplexed with C1-C2.

Automated smFISH and IHC

All histology on mouse and human brain cryosections was automated on a Leica BOND RX robotic stainer after manual baking and dehydration. Tissue sections were first processed for 3 or 4 gene smFISH using the RNAScope LS Multiplex Assay (ACD). After smFISH, antibody staining was performed using TSA and slides were manually coverslipped for imaging.

i. Baking and dehydration: Tissue cryosections were removed from -80ºC and thawed at RT for 15 min. Samples were then baked at 65ºC for 45 min in vertical position on a slide holder (Tissue-Tek) in an oven. After baking, samples were dehydrated in a series

of 50%, 70%, 100% and 100% ethanol (5 min each) in staining dishes (Tissue-Tek) and air-dried for 10 min before automated RNAScope.

ii. Automated histology design and setup: For use on the Leica BOND RX, all histology consumables were transferred to barcoded reagent containers. Staining protocols that list the order and durations of reagent incubations and washes were created on the BOND controller software. Slides were assigned unique barcode labels coupled to staining protocols and placed onto temperature-controlled pads on the instrument. Flow-through chambers were assembled across the whole slides using plastic coverplates. During staining, a liquid volume of 150 µL was dispensed to each slide on every step using automated liquid handling. Reagents were flushed at least once before main incubations to ensure uniform coverage of the slide. Between reagent incubations, multiple short washes were performed. All incubations were performed at room temperature unless indicated otherwise. For the 4-plex RNAScope smFISH protocol, a maximum number of 20 slides could be processed against 10 different probe mixtures in a single run (e.g. 40 different genes screened across two sets of biological replicates). The combined multiplexed RNAScope smFISH and IHC protocol for 20 slides ran overnight on the Leica BOND RX lasting ~17 hours.

iii. Automated RNAScope smFISH: The RNAScope LS Multiplex assay (ACD) was performed largely according to the instructions from the vendor and modifications are noted below. Full details of the protocols 4-plex smFISH and the consumables used in this study are provided in Supplementary Table 4.

4-plex probe hybridization: To perform 4-plex RNAScope on mouse brain cryosections, samples were initially permeabilized with heat and protease treatment to improve probe penetration and hybridization. For heat treatment, P14 and P56 samples were incubated in BOND ER2 buffer (pH 9.0, Leica) at 95°C for 2 and 5 min, respectively. For protease treatment, P14 and P56 samples were incubated in ACD protease reagent at 42°C for 10 and 15 min, respectively. Prior to probe hybridization, samples were incubated in hydrogen peroxide for 10 min to inactivate endogenous peroxidases and ACD protease. Following pre-treatment, samples were incubated in target z-probe mixtures (C1-C4) for 2 h at 42°C. The C2-C4 probes are provided at 50X concentration by ACD and were diluted 1:50 in C1 probes. In exception, the C4 probe for the high-expressing *Glast* mRNA was used at 1:100 in the astrocyte screen for reagent conservation.

smFISH signal amplification: After probe hybridization, branched DNA amplification trees were generated through sequential incubations in AMP1, AMP2 and AMP3 reagents for 15-30 min each at 42°C with LS Rinse buffer high stringency washes between incubations. Following amplification, probe channels were detected sequentially via HRP-TSA labeling. To develop the C1-C3 probe signals, samples were incubated in channel-specific HRP reagents for 15 min at 42°C, TSA fluorophores for 30 min and HRP blocking reagent for 15 min at 42°C. The probes in C1, C2 and C3 channels were labeled using Opal 520, 570 and 650 fluorophores (Perkin Elmer, diluted 1:2500) respectively. Finally, to develop the C4 probe, the Atto425 fluorophore was used for 6-color imaging on the Operetta system. The C4 probe complexes were first incubated with TSA-biotin (Perkin Elmer, 1:500) for 30 min, followed by streptavidin-conjugated

Atto425 (Sigma, 1:400) for 30 min. Multiple short washes were performed between incubations throughout the protocol using the BOND Wash buffer (Leica) and deionized water (full protocol listed on Supplementary Table 4).

3-plex smFISH: To perform 3-plex RNAScope on human brain cryosections, samples were heat-treated for 10 min and incubated in protease for 15 min. Probe hybridization and branched DNA amplification were performed as described above. To develop C1-C3 probes, Opal fluorophores (520, 570 and 650) were used at a lower dilution (1:300) due to higher autofluorescence on postnatal human brain sections. To distinguish RNA spots from lipofuscin autofluorescence, spots that appear identical across Opal 520 and 570 channels were filtered out.

iv. Automated immunohistochemistry: RNAScope smFISH was directly followed by antibody staining for the neuronal marker NEUN on the BOND RX system. To improve antibody staining after IHC and perform 6-color imaging on the Operetta, the NEUN signal was amplified using TSA-biotin and the Alexa 700 fluorophore. Samples were first blocked in antibody blocking solution (Perkin Elmer) for 20 minutes. To block any available TSA-biotin sites from the smFISH assay, samples were incubated in 0.2% Avidin (Sigma) for 20 min and 0.05% Biotin (Sigma) for 30 min. After the avidin-biotin block, samples were incubated in chicken anti-NEUN antibody (Milipore) diluted 1:500 in blocking solution for 1 hr. To develop the antibody signal, samples were incubated in goat anti-chicken HRP (ThermoFisher, 1:500) for 1 hr, TSA-biotin (1:200) for 10 min and streptavidin-conjugated Alexa 700 (Sigma, 1:200) for 30 min. Following antibody staining, samples were incubated in DAPI (Sigma, 0.25 µg/ml) to mark cell nuclei and washed multiple times in deionized water. After final washes, slides were briefly air-dried and manually mounted using ~170 µL of Prolong Diamond Antifade (Fisher Scientific) and standard coverslips (24x50 mm; Fisher Scientific). The full IHC protocol is listed under Supplementary Table 4.

Automated spinning disk confocal imaging

Tissue sections were imaged on an Operetta CLS high-content screening microscope (Perkin Elmer). To perform 6-color smFISH-IHC imaging, this system was equipped with 8 LED light sources, 5X air and 40X water objectives, wide-field and spinning disk confocal imaging modules and narrow band emission filters. The fluorophores, light sources, exposure times and emission filters used for mouse and human tissue imaging experiments are listed in Supplementary Table 5. Image acquisition and analysis were controlled using the Harmony software (Perkin Elmer).

i. Tissue identification: To locate whole tissue sections or ROIs for high-resolution imaging, entire slides were initially scanned under low magnification in wide-field mode. Each slide was imaged for nuclear DAPI and NEUN staining if applicable using a 5X NA 0.16 objective (pixel size: 7.2 µm) under 5 minutes. To automatically locate the xy-coordinates of tissue sections, a Harmony analysis script was used to detect DAPI+ areas. Whole slide DAPI images were stitched, smoothed with Gaussian blurring and analyzed with a global threshold. The detected DAPI+ areas were size filtered to remove staining artifacts and slightly expanded to ensure complete tissue coverage. The resulting areas were used to automatically set the xy-field positions of the subsequent 40X scan.

Alternatively, ROIs for 40X scans were manually selected on low magnification previews. Selected 40X fields were imaged with a 7% overlap.

ii. Confocal imaging: The high-resolution smFISH images of tissue sections were acquired on the spinning disk confocal mode using a sCMOS camera and a 40X NA 1.1 automated-water dispensing objective. The field-of-view was 320 x 320 µm and the pixel size was 298 nm. A P14 mouse brain hemisection comprised 200 to 300 fields depending on its anatomical position. Each field was imaged as a z-stack consisting of 20 to 30 planes with a 1 µm step size across each color channel. An IR laser was used to auto-focus on the position of the coverslip and the relative z-heights of tissue sections were manually identified by imaging DAPI on sample fields prior to tissue-wide scans. Each z-plane was imaged across 4-6 channels depending on the experiment with exposure times for mouse smFISH channels between 60 and 120 ms (Supplementary Table 5). The 40X multi-channel settings and tissue heights were entered into an experimental layout on Harmony and automatically executed after low magnification tissue identification scans.

Image analysis

To segment single neurons and astrocytes and quantify RNA spots from high-resolution images, analysis scripts were created on Harmony software (Perkin Elmer) using customizable pre-defined function blocks (*italicized below*). The complete single neuron and astrocyte segmentation pipelines are provided in Supplementary Tables 6 and 7. Each 40X field was analyzed separately to optimize processing time of large datasets.

i. Quantification of neuronal gene expression *in situ*:

a. Segmentation of neurons: Maximum intensity z-projection images were calculated across each channel to generate 2D images from z-stacks. NEUN+ neurons were segmented in three steps. **1**) Supervised texture segmentation was performed at a coarse scale to locate NEUN+ areas on images and filter staining artifacts on tissue sections (*find texture regions*). Intensity and size thresholding then identified the NEUN+ neuronal soma (*find image region*). **2**) Neuronal nuclei were segmented within the NEUN+ soma from Gaussian blurred DAPI images using intensity, size and contrast thresholds (*find nuclei*). **3**) The neuronal cytoplasm was segmented around the nuclei within the boundaries of the neuronal soma using NEUN intensity thresholding (*find cytoplasm*).

b. Filtering single neurons: Neuron segmentation yielded single neurons as well as doublets/triplets that overlap in z-projection images and neurons that are partially contained in tissue sections (Supplementary Figure 1B). To automatically distinguish single neurons, morphological (e.g. area, roundness) and intensity (e.g. pixel sum over DAPI and NEUN) properties of segmented cells were measured and used to train a supervised linear classifier (*select population*). For the training set, we manually selected more one hundred single, doublet and partial cells across multiple tissue sections and cortical areas. The resulting classification was validated across the cortex by manual inspection of several fields.

c. RNA spot calling in neurons: RNA spots were identified by the detection of local intensity maxima across each smFISH channel in the neuronal soma (*find spots*). Individual spots were identified with an upper radius threshold of 750 nm. The number of RNA spots per single neuron was calculated for each smFISH channel (*calculate properties*). Last, all DAPI+ nuclei were identified across the given field for use in brain region segmentation (see anatomical annotation below).

ii. Quantification of astrocyte gene expression *in situ*:

a. Segmentation of astrocytes: Maximum intensity z-projection images were generated as above. Background illumination profiles of fluorescent channels were mapped to correct uneven illumination (*flatfield correction*). *Glast*+ astrocytes were segmented in three steps: **1**) Supervised texture segmentation was performed at a fine scale to identify *Glast*+ astrocyte cytoplasm and main processes (*find texture regions*). To train texture analysis, over a hundred points were selected inside versus outside *Glast*+ cortical astrocytes across several tissue sections. Astrocyte cell areas were then filtered by size to remove partial cells and holes across astrocyte nuclei, which are weakly labeled by *Glast* smFISH, were filled (*select region*). **2**) Astrocyte nuclei were segmented within *Glast*+ cell areas from Gaussian blurred DAPI images using intensity, size and contrast thresholds (*find nuclei*). To remove false positive non-astrocyte nuclei that overlap with astrocyte processes in z-projections, additional morphology and Glast intensity filters were used (*select population*). **3**) The astrocyte cytoplasm and processes were segmented around the nuclei within the cell areas using *Glast* intensity thresholding (*find cytoplasm*).

b. Filtering single astrocytes: To remove overlapping astrocyte doublets and partial cells, cells were filtered based on morphological (e.g. area, roundness) and intensity (e.g. pixel sum over DAPI and *Glast*) properties. As shown in Supplementary Figure 11, upper layer astrocytes were slightly larger consistent with previous reports (*7*) and showed higher *Glast* levels than those in deep layers. This analysis identified similar numbers of astrocytes across cortical areas in technical replicates (Supplementary Figure 11). Manual validation of this pipeline across ten tissue sections from two biological replicates covering multiple cortical areas (somatosensory, visual, auditory) showed that >90% of astrocytes were correctly identified using this pipeline.

Given their intimate cell-cell interactions, astrocyte processes occasionally overlapped with neuronal soma and other nuclei in maximum-z projection images. To remove overlapping non-astrocyte nuclei, the DAPI signal in the astrocyte cytoplasm was identified with intensity thresholding and subtracted from the *Glast*+ cell area (cytoDAPI filtered cells, Fig 2C). To remove overlapping neurons, NEUN signal was used to segment neurons as above. Astrocytes that significantly overlap with neurons were discarded (>50% overlap between the astrocyte nuclei and neuronal soma). NEUN+ neurons were then subtracted from the cytoDAPI-filtered Glast+ cell area (Fig 2C), resulting in astrocytes filtered against overlapping neurons and nuclei.

c. RNA spot calling: RNA spots were quantified across single astrocytes as elaborated for neuron previously. In addition to the filters used above, cells that are high-expression

outliers (above 99.5% of spot counts per gene across the brain) were also filtered out. RNA spots in neurons, cytoDAPI-filtered and double-filtered astrocytes were also quantified.

iii. Data processing:

The analysis was performed on a desktop workstation with two 6-core Intel i7-4930K 3.4 GHz CPUs and 64 GB of RAM. The neuronal dataset shown in Fig 1, consisting of 10 tissue sections and ~300,000 images, was analyzed under 6 hours. The data was exported from Harmony as a single cell matrix showing cell coordinates, morphological and intensity measurements, and RNA spot counts per cell. Brain region segmentation was performed in MATLAB (described below). Data organization and plotting were done in R.

Anatomical annotation of mouse cortical layers and areas

For mapping neuron and astrocyte subtypes across the cortex, one P14 mouse brain hemisphere was sectioned along the coronal plane to generate an 8-slide series containing 10 sections each. One slide was used to map the expression of cortical layer neuron markers (Fig 1) and the remaining slides were assayed with layer astrocyte markers (Fig 3 and 6). The cortical layers and areas were annotated using NEUN and DAPI staining as well as layer neuron marker expression patterns as anatomical landmarks (see Supplementary Figure 7 for areas). The Paxinos (*P6, plates 9 to 40*) and Allen Mouse Brain ISH Atlases (*P56, sections 38 to 88*) were used as anatomical references. Cortical areas were annotated broadly across the anterior-posterior and dorso-ventral axes, grouping functionally related areas (e.g. the anterior division of the somatosensory cortex contains the mouth and limb areas). The list of cortical area abbreviations and groupings are listed under Sup Table 8.

For screening layer astrocyte gene expression (Fig 2), two P14 mouse brain hemispheres (biological replicates) were sagitally sectioned to generate 18 slides. Each slide contained 4 sections through the somatosensory cortex from each replicate, corresponding to the areas used for RNAseq profiling of layer astrocytes.

For examining cortical layers in *Satb2* cKO and *Reeler* mice (Fig 5), three coronal sections through the somatosensory barrel cortex were collected from littermate control and mutant brains (n=3 biological replicates each). Each slide contained sections from one control and one mutant brain.

To normalize the layer depth of neurons across cortical areas, we automatically measured the normalized distance between individual neurons, cortical pia and white matter using the slideSegmenter application below.

Manual segmentation of brain regions

Brain areas were manually segmented on low magnification (5X) images of DAPI/NEUN stained brain sections. These segmentation masks were overlaid on xy-coordinates of high-magnification (40X) scans to annotate single cells. The offset between 5X and 40X objectives was manually corrected by aligning DAPI+ nuclei (identified across all cells in each field at the end of segmentation pipelines). To stitch images from Harmony, draw and name segmentation masks, align low-high magnification data and perform batch segmentations, the slideSegmenter application was created to work on the MATLAB

environment and made publicly available (https://bitbucket.org/alexmatlab/slidesegmenter/).

Identification of neuronal subtypes from smFISH data

To identify cortical neuron subtypes in an unbiased manner from smFISH data, we adopted the following workflow:

i. Filtering and normalization: For downstream analysis, neurons were 1) selected from the 8 broad cortical areas that show the full complement of layers with respect to the 4 genes profiled; and 2) filtered with a minimum cumulative spot-count threshold of 20. Spot counts then had a value of 1 added and were log transformed (log(spot counts +1)).

ii. Clustering: Clustering was performed for cells from each region individually with the 4 genes profiled using graph-based clustering implemented by Seurat (FindClusters function, resolution 0.5) (41). Briefly, a K-nearest neighbor graph based on Euclidean distance is constructed from the expression values for each cell. Edges between cells were weighted based on shared overlap in neighborhoods determined by Jaccard distance. Cells were iteratively grouped together with the goal of optimizing the density of links inside communities as compared to links between communities.

iii. tSNE: For visualization, t-distributed stochastic neighbor embedding (tSNE) coordinates were calculated from the expression values for each cell (independent of the clustering) using perplexity 250 with Seurat (RunTSNE function). tSNE plots were then colored by the cluster assignments derived above, gene expression values, or other features of interest.

iv. Hierarchical clustering: The mean expression profiles of each of the Seurat clusters derived from each brain region were taken and hierarchically clustered together based on Euclidean distance using Ward.D2 clustering (hclust(dist, method = "ward.D2") R function). The resulting dendrogram was then cut at height 1.9 yielding 18 groups (cutree(hc, h = 1.9) R function). These groups were manually annotated to 10 major subtypes based on high expression differences (Supplementary Figure 5) and similarity among the spatial distributions of identified groups.

Cortical layer and purified layer astrocyte RNA-Seq

i. Cortical layer dissection: *Aldh1L1-GFP*+ mice were transcardially perfused at P14 with ice-cold Hanks Balanced Solution (HBSS) to wash away the blood. Brains were dissected and cortical hemispheres were cut sagitally on a vibratome in ice-cold HBSS to 300 µm thick sections. Sections from 8 littermate pups were pooled for each experiment (n=3 biological replicates for astrocyte purification and n=2 biological replicates for whole layer RNA extractions) and microdissected to separate upper (L2-4) and deep (L5-6) cortical layers. The L4 of the somatosensory barrel cortex, which appears as dark barrels separated by light septa under bright-field illumination, was used as an anatomical landmark for layer microdissections (Supplementary Figure 8). To prevent contamination

with white matter astrocytes, the most superficial layers that contain pial and L1 astrocytes, and the deep subcortical white matter that contains fibrous astrocytes were discarded. For each experiment, the dissections were completed under 90 min and the tissue was kept in ice-cold HBSS.

ii. Flow cytometry: To purify cortical layer astrocytes, tissue dissociation was performed as described previously (17). Briefly, cortical layer tissue were minced with a forceps and enzymatically dissociated with papain (20 U/mL) in dissociation buffer (glucose 22.5 mM, EDTA 0.5 mM, phenol red), L-cysteine (1 mM) and DNase (125 U/mL) for 80 min at 33ºC. Tissue was then washed in inhibitor solution (dissociation buffer with ovomucoid (1.0 mg/mL)) and centrifuged for 5 min at 200 g. Supernatant was discarded, the tissue was resuspended in the inhibitor buffer and mechanically disrupted using a P1000 pipette. Dissociated cells were layered onto inhibitor buffer with concentrated ovomucoid (5 mg/mL) and centrifuged 5 min at 200 g. Finally, the cell pellet was resuspended in staining medium with DAPI. *Aldh1l1-GFP*$^{+}$ and *Aldh1l1-GFP*$^{-}$ cells were sorted as previously described (8) on a BD FACS Aria II and gated on forward/side scatter, live/dead by DAPI exclusion, and GFP, using GFP and DAPI controls to set gates for each experiment (Supplementary Figure 8).

iii. RNA sequencing and analysis: Total RNA from FACS-purified cortical layer astrocytes and whole cortical layers was extracted with Trizol LS (Invitrogen) and purified using the RNeasy Kit (Qiagen). cDNA was generated from full-length RNA using the NuGEN RNA-Seq V2 kit that employs the single primer isothermal amplification method to deplete ribosomal RNA, and sheared by Covaris to yield uniform size fragments. RNASeq libraries were generated using the NuGen Ultralow kit for adapters, barcoding, and amplification and purified using the Agencourt XP magnetic beads, quality controlled with an Agilent bioanalyzer, and quantified by qPCR.

Five libraries were pooled per lane across three lanes for single end (SE50) sequencing on a HiSeq 4000. Read quality was assessed using FastQC (version 0.11.4) and 5 nucleotides at the 5' end were trimmed. 45 nucleotide long reads were aligned to the mouse reference genome (Ensembl GRCm38) using TopHat2 (version 2.0.11) (42). The multiple hit parameter was (-g) was set to 1 to exclude reads with multiple genomic alignments. On average, 68 million reads were uniquely mapped to each sample (range 59-87M). Read counts per gene were calculated using SAMtoools (version 0.1.19) (43) and HTSeq (version 0.6.1p1) with default parameters (44). DESeq2 (45) was used to detect differentially expressed genes amongst upper and deep layer astrocytes (n=3 biological replicates) and whole cortical layers (n=2 replicates). Purified deep layer astrocytes showed low levels of contaminating oligodendrocyte marker gene expression (e.g. MBP); these genes were excluded from analysis using a mild astrocyte-specific expression threshold (astrocyte vs whole layer expression > 0.1). To identify the top differentially expressed genes between upper and deep gray matter astrocytes, an expression threshold of 5 FPKM was used with a false-discovery rate (FDR) < 0.05. The resulting list of 159 differentially expressed layer astrocyte genes is provided in Supplementary Table 9.

Spatial reconstruction of astrocyte layer heterogeneity:

i. Pre-processing of astrocyte scRNA-seq data: Single cell RNA-sequencing data of P56 cortical astrocytes was obtained from Batiuk and Martirosyan et al (23) which used a modified version of Smart-seq2 protocol. Number of unique molecules (UMI) was estimated from raw read counts with Census method from Monocle package (46). UMI version of the data was normalised with size factors according to standard scater workflow (47).

ii. Spatial reconstruction: We reconstructed spatial profiles of genes measured with scRNA-seq using a published method (22). Implementation of the method in Matlab was provided by Shalev Itzkovitz, see original publication for the description of implementation details. Here we summarize the method.

a. Constructing the prior on the number of reads for markers genes in scRNA-seq cells: Molecule counts of genes from the processing step of image analysis were fit by a Gamma distribution for each gene i and spatial bin j.

(1) $sc_{ij} = Gamma(os_{ij}, or_{ij})$

Where sc is spot counts, os is observed shape of gamma distribution, and or is observed rate.

To match this distribution to the statistical properties of scRNA-seq data and produce the prior distribution of scRNA-seq reads for each gene i and spatial bin j the following correction was applied for each scRNA-seq cell c:

(2) $f_c = (\frac{s_c}{sm})$

Where f is the distribution rescaling factor, s is scRNA-seq sampling constant, sm is smFISH sampling constant

(3) $p_{ijc} = \frac{f_c}{(\mathrm{or}_{ij} + f_c)}$

where p is negative binomial probability

(4) $prc_{ijc} = NegativeBinomial(r = os_{ij}, p_{ijc})$

Where prc is the prior on expected single cell RNA-seq reads for each marker gene, bin and cell

smFISH sampling factor reflects the expected proportion of the total number of transcripts in a cell captured in smFISH images (we used 0.15). scRNA-seq sampling factor reflects the proportion of total number of transcripts (approximated as 180000) captured by scRNA-seq for each cell measured. The total number of transcripts was chosen based on Halpern et al that examined haptocytes: 180000 is roughly 1/4 of hepatocyte molecule number: 1/2 to account to tetraploidy and 1/2 to account for smaller cell size of astrocytes. In practice, sampling levels are computed for 8 bins of cells with similar sampling levels (e.g. 0-0.1%, 0.1%-0.3% …) to speed up the Monte Carlo

sampling used to construct the prior. We used 5 spatial bins (j) for equally sized intervals of cortical depth.

b. Using the prior to assign cells to spatial bins. To find the probability of each scRNA-seq cell coming from spatial bin j given the expression of spatial markers we used Bayes' formula:

$$(5)\ P(Bin_j \mid gene_i\ reads) = \frac{P(gene_i\ reads \mid prc_{ijc}) * P(cells\ in\ Bin_j)}{\sum_{bin\ j=1}^{bin\ 5} P(gene_i\ reads \mid prc_{ijc}) * P(cells\ in\ Bin_j)}$$

where $P(cells\ in\ Bin_j)$ is the proportion of cells in spatial bin j, and the prc prior on reads comes from Equation (4).

The method assumes that expression of different genes is independent and the probability of assignment to spatial bins is computed as:

$$(6)\ P(Bin_j \mid gene_{i-n}\ reads) = \prod_{gene\ i=1}^{gene\ n} P(Bin_j \mid gene_i\ reads)$$

This result in posterior probability matrix of cells by bins. A probability weight matrix is obtained by normalizing the column sums to one

c. Reconstructing expression of genes across spatial bins. The probability weight matrix, P and the scRNA-seq expression matrix, E, are combined to obtain spatial profiles as a genes by bins matrix as a weighted average (Supplementary Tables 10 and 11).

$$(7)\ S = E * P$$

d. Identifying significantly zonated profiles. To find which profiles are significantly zonated we assigned cells to the spatial bin with highest posterior probability. The Kruskal–Wallis test was used to find which genes are significantly different between cells assigned to different spatial bins.

e. Leave one out validation. To benchmark the model we used leave one out analysis (Supplementary Figure 18). We used 15 genes with smFISH profiles to reconstruct one left-out gene and compared the reconstructed profile to the average expression observed with smFISH. To measure the similarity of predicted and observed profiles we used Kullback–Leibler divergence base on the relative differences in expression between spatial bins rather than absolute number of genes per bin.

Manual immunohistochemistry:

Cryosections from *Aldh1L1-GFP* mice were manually stained for GFP, astrocyte and neuron marker antibodies. Samples were subjected to heat-induced antigen retrieval in 10mM sodium citrate (pH 6) buffer for 5 min at 75ºC, then permeabilized and blocked in 10% goat serum in 1X PBS with 0.1% Triton X-100 (PBST) for 1 h. Primary antibodies

were diluted in the blocking solution and incubated O/N at 4ºC. After multiple PBST washes, samples were incubated in secondary antibodies and DAPI diluted in blocking solution for 1 h. After PBS and dH_2O washes, samples were mounted using Fluoromount-G (SouthernBiotech). The following primary antibodies were used: chicken GFP (GFP-1020, Aves, 1:2000), mouse NEUN (MAB377, Millipore, 1:500), rabbit GS (G2781, Sigma, 1:2000) and rabbit pSmad (13820S, Cell Signaling, 1:200). Goat secondary antibodies conjugated to Alexa fluorophores (Molecular Probes) were used for labeling. The *Aldh1L1-GFP* samples were imaged on a Leica TCS SPE laser confocal microscope with a 40x oil immersion objective.

Statistics:

The violin plots in Figure 1D, Supplementary Figures 2B-C, 11C and 21C and the box plots in Supplementary Figure 20A-B were plotted to show the data distribution as follows. The lower, middle and upper hinges correspond to 25, 50 (median) and 75 percentiles. The whiskers show data points within 1.5 times the interquartile range (distance between the first and the third quartiles) of the 25 and 50 percentiles.

No statistical methods were used to pre-determine sample sizes but our sample sizes are similar to those reported previously (10-12). smFISH data (RNA spot counts per cell) and scRNAseq data distribution was assumed to be Gamma-Poisson but this was not formally tested.

For layer switch experiments (Figure 5), data collection and analysis were performed blind to the genotypes of the animals. Animals were randomly allocated to experimental groups. Two-tailed Student's t-tests were used to assess statistical significance in layer switch experiments (Figure 5).

Data Availability:

The raw bulk RNA-sequencing data are available at the Gene Expression Omnibus (GEO) under the accession code GSE140822. The single cell RNA-sequencing data will be made available under https://holt-sc.glialab.org/sc/. Other data are available as Supplementary Materials or from the corresponding author upon request.

Code Availability:

The code for spatial reconstruction of single cell astrocyte RNA-sequencing can be found at https://github.com/vitkl/cortical_astrocyte_mapping. The SlideSegmenter code is available at https://bitbucket.org/alexmatlab/slidesegmenter/src/master/. The Harmony image analysis scripts are provided as Supplementary Materials. Other code is available upon request.

Supplementary Methods References:

37. Gong S, Zheng C, Doughty ML, Losos K, Didkovsky N, Schambra UB, et al. A gene expression atlas of the central nervous system based on bacterial artificial chromosomes. Nature. 2003 Oct 30;425(6961):917–25.

38. Gorski JA, Talley T, Qiu M, Puelles L, Rubenstein JLR, Jones KR. Cortical Excitatory Neurons and Glia, But Not GABAergic Neurons, Are Produced in the Emx1-Expressing Lineage. Journal of Neuroscience. Society for Neuroscience; 2002 Aug 1;22(15):6309–14.

39. Wang F, Flanagan J, Su N, Wang L-C, Bui S, Nielson A, et al. RNAscope. The Journal of Molecular Diagnostics. 2012 Jan;14(1):22–9.

40. Kerstens HM, Poddighe PJ, Hanselaar AG. A novel in situ hybridization signal amplification method based on the deposition of biotinylated tyramine. J Histochem Cytochem. 1995 Aug 4;43(4):347–52.

41. Butler A, Hoffman P, Smibert P, Papalexi E, Satija R. Integrating single-cell transcriptomic data across different conditions, technologies, and species. Nat Biotechnol. Nature Publishing Group; 2018 Jun;36(5):411–20.

42. Kim D, Pertea G, Trapnell C, Pimentel H, Kelley R, Salzberg SL. TopHat2: accurate alignment of transcriptomes in the presence of insertions, deletions and gene fusions. Genome Biol. BioMed Central; 2013 Apr 1;14(4):R36.

43. Li H, Durbin R. Fast and accurate short read alignment with Burrows-Wheeler transform. Bioinformatics. 2009 Jul 15;25(14):1754–60. PMCID: PMC2705234

44. Anders S, Pyl PT, Huber W. HTSeq—a Python framework to work with high-throughput sequencing data. Bioinformatics. Oxford University Press; 2015 Jan 15;31(2):166–9.

45. Love MI, Huber W, Anders S. Moderated estimation of fold change and dispersion for RNA-seq data with DESeq2. Genome Biol. BioMed Central; 2014 Dec 1;15(12):550.

46. Qiu X, Hill A, Packer J, Lin D, Ma Y-A, Trapnell C. Single-cell mRNA quantification and differential analysis with Census. Nat Methods. 2017 Jan 23. PMCID: PMC5330805

47. Lun ATL, McCarthy DJ, Marioni JC. A step-by-step workflow for low-level analysis of single-cell RNA-seq data with Bioconductor. F1000Research. Faculty of 1000 Ltd; 2016;5:2122. PMCID: PMC5112579

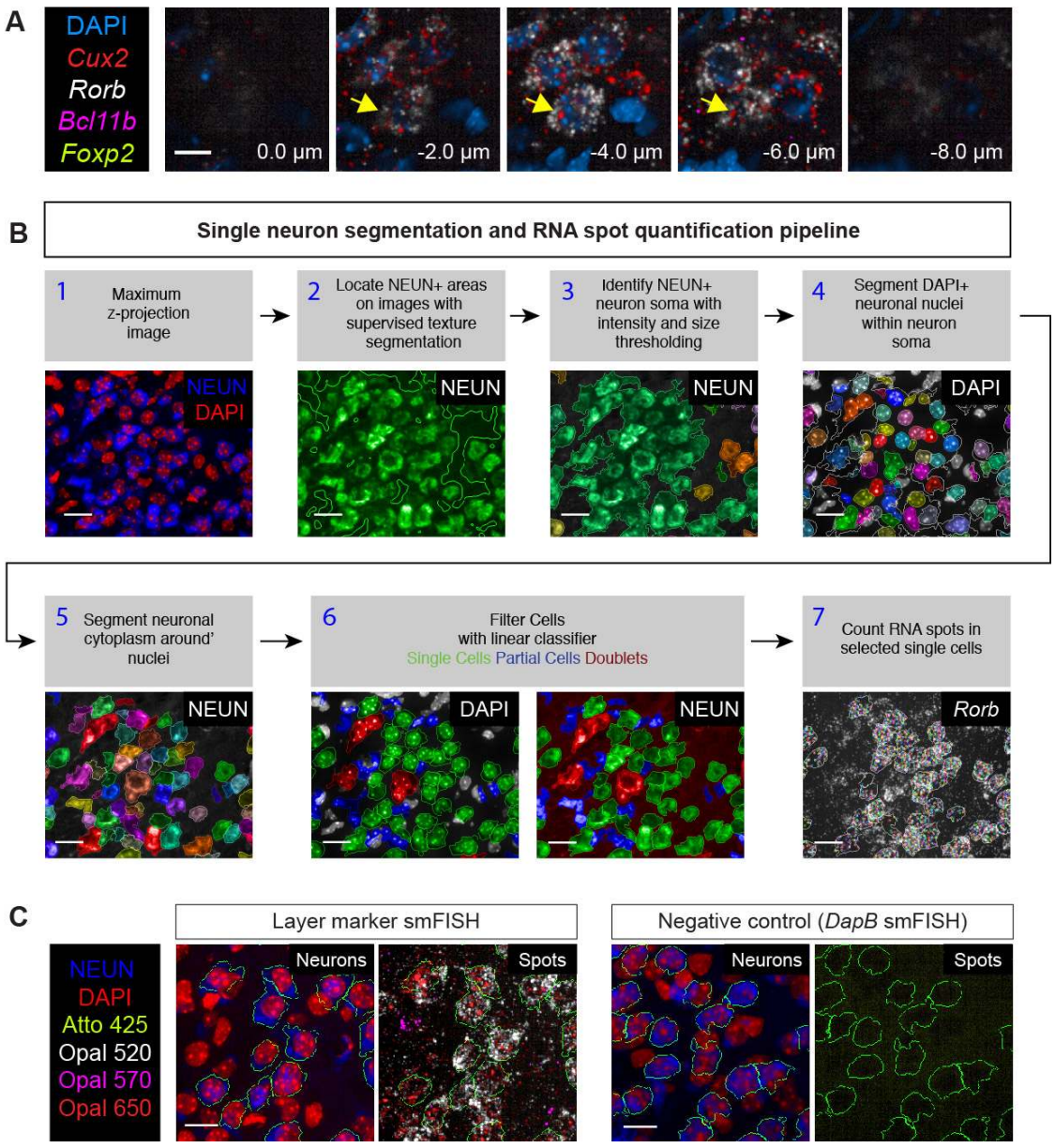

Supplementary Figure 1: Single neuron image analysis and gene expression quantification pipeline.

A) Individual 40X z-planes throughout *Rorb*$^{+}$ L4 neurons. Arrow indicates a single neuron across multiple z-positions. Nuclei are marked by DAPI. For neuronal segmentation, the z-stack is collapsed into a single plane via a maximum intensity projection.

B) Segmentation of NEUN+ neurons and quantification of gene expression in single neurons.

C) RNAScope smFISH assay shows high signal-to-noise ratio. The background signal is assessed by comparing smFISH against layer neuron markers to bacterial *DapB* transcript negative control (targeted with four different probes in different channels). *DapB* smFISH shows little to no signal on mouse tissue sections, as expected. Quantification shown in Supplementary Figure 2. *n*=12 mice independently assayed, 3-10 tissue sections per replicate imaged.

Scalebars: (A) 10 µm, (B,C) 20 µm

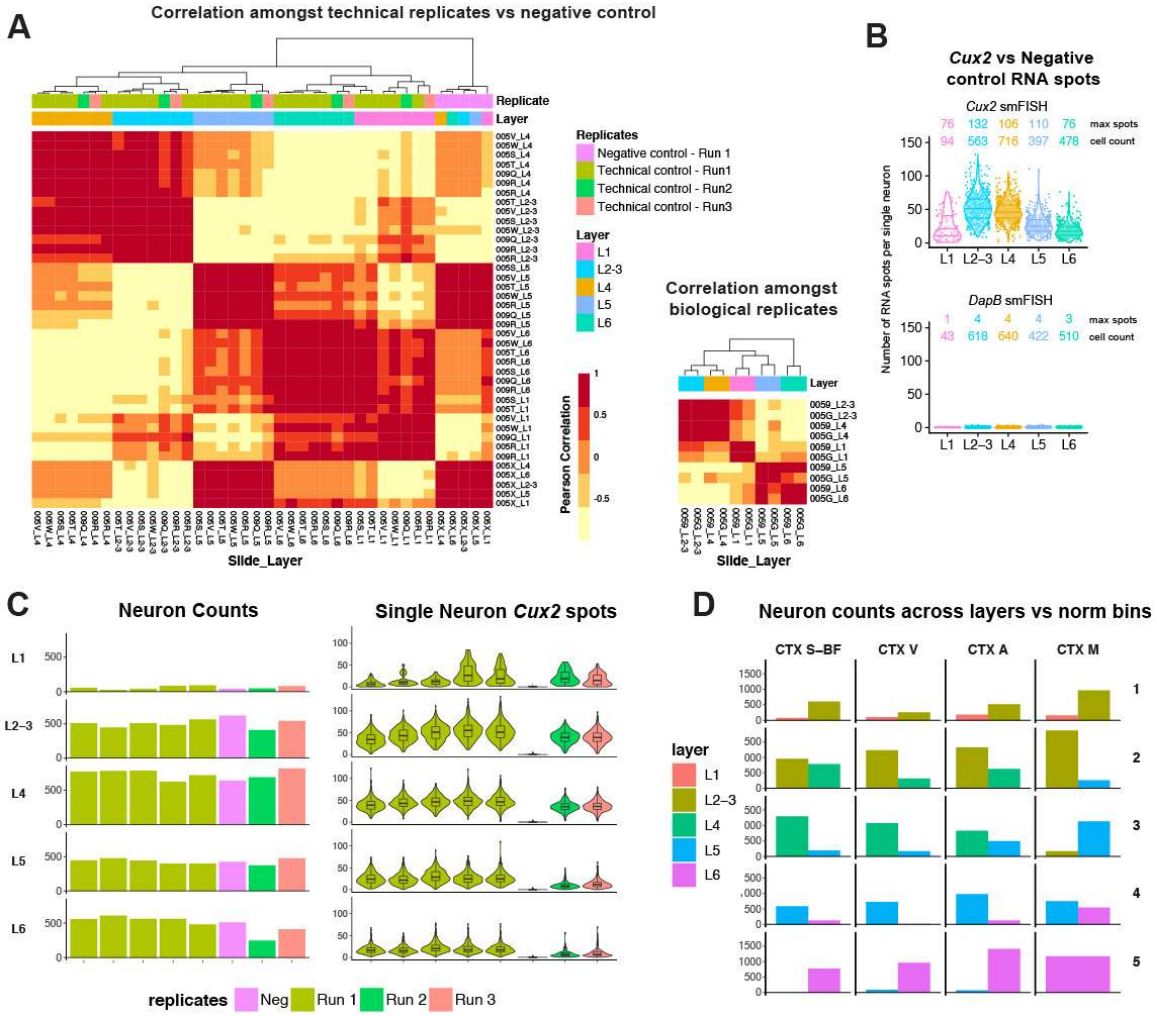

Supplementary Figure 2: Reproducibility of single neuron gene expression measurements. **A)** Neuronal gene expression measurements are highly consistent across technical and biological replicates. (Left) Heatmap showing the pearson correlation values across expression profiles of technical replicates and the negative control. Technical replicates are consecutive P14 brain sections on different slides assayed for smFISH against 4 layer markers. Negative control was assayed for smFISH against bacterial *DapB* transcripts. To assess technical variation within a staining run, multiple replicates were assayed simultaneously on the BOND RX (Run 1). To assess batch effects, replicates were assayed on different days using different consumable reagent kits (Runs 2 and 3). To calculate the expression profiles of replicates per cortical layer, single neuron RNA spot counts for 4 layer markers (*Cux2, Rorb, Bcl11b, Foxp2*) are averaged and log-transformed across each layer (L1, L2-3, L4, L5, L6) in the barrel cortex. The replicate-layer expression profiles were then hierarchically clustered. As expected, cortical layers clustered across technical replicates from the same staining run as well as different batches, indicating reproducibility, while negative control layers formed a distinct cluster. (Right) Heatmap showing the pearson correlation values across expression profiles of biological replicates. Biological replicates are barrel cortex sections from two littermate P14 animals. Average layer expression profiles were calculated as described above. As expected, cortical layers from biological replicates clustered together.

B) Quantification of single neuron Cux2 vs negative control *DapB* expression across cortical layers. The background signal of RNAScope smFISH, assessed by the numbers of *DapB* spots per cell, is 0 to 2 spots per cell. Dot plot and the violin plot show single cell data. n=2 mice independently assayed, 3 tissue sections imaged.
C) (Left) Quantification of neurons across cortical layers in the barrel cortex amongst replicates. Similar number of neurons are detected based on NEUN IHC and DAPI staining across technical and negative replicates. (Right) Quantification of single neuron *Cux2* expression across technical and negative replicate with violin and boxplots. Negative control shows the quantification of *DapB* expression in the same probe channel used for *Cux2* (Opal 650). The range of single cell *Cux2* expression across upper layers is highly consistent amongst technical replicates from the same staining run. Slightly lower expression is observed on batch replicate controls, yet the upper layer enrichment of Cux2 is highly similar. *n*=1 mouse, 3 tissue sections independently imaged.
D) Distribution of layer neurons across normalized cortical depth bins. Cortical layers were manually annotated across four cortical areas, then neurons were sorted into five bins across normalized cortical depth between the pial surface and the white matter. The distributions of layer neurons to depth bins is largely similar across different cortical areas, with the exception of motor cortex that lacks a prominent layer 4.

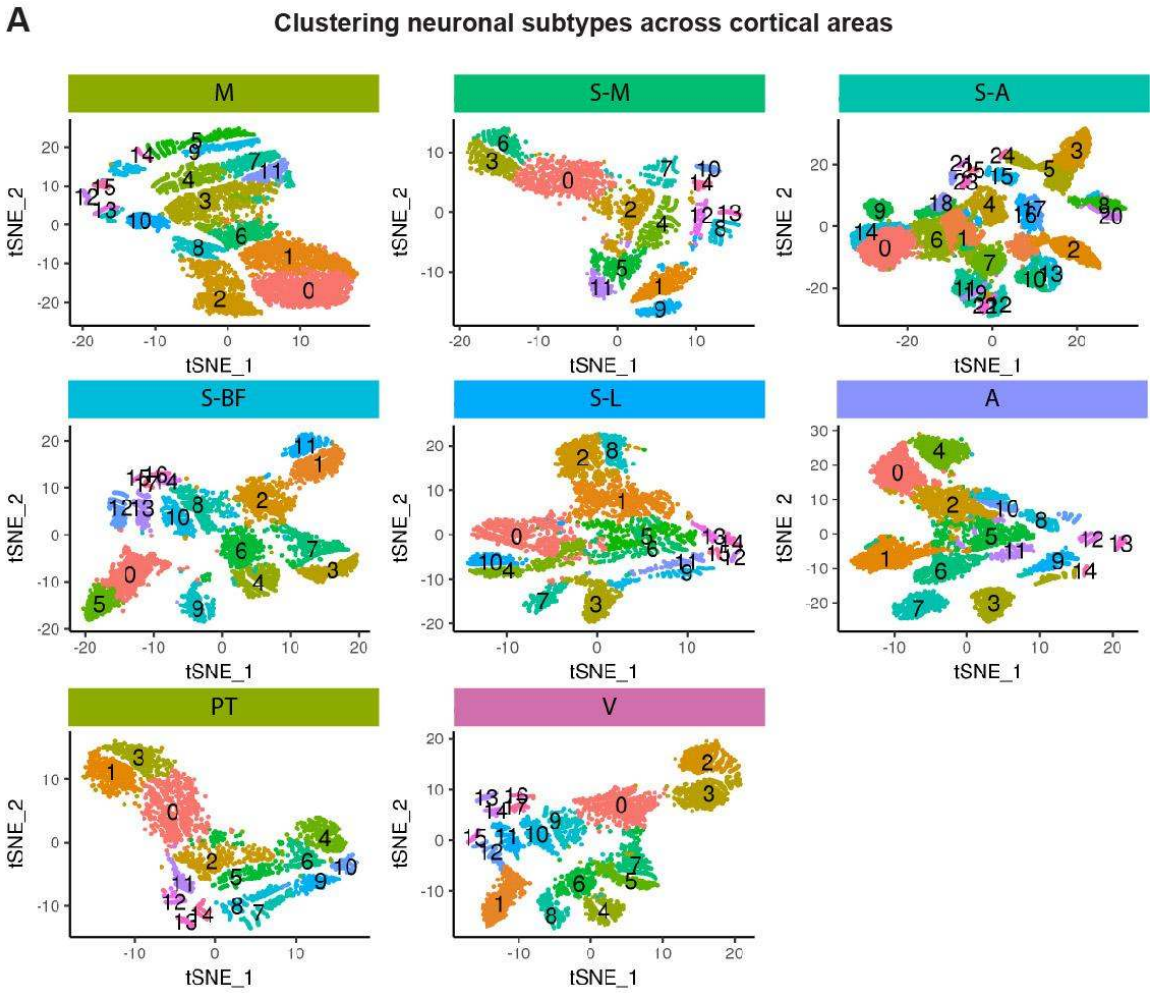

Supplementary Figure 3: Clustering of single neurons from different cortical areas. **A)** To identify neuronal subtypes, clustering of single neuron gene expression was performed within each cortical area individually with 4 layer markers profiled. Single neuron tSNE coordinates were calculated from the expression profiles and tSNE plots were colored according to cluster assignments from above. See Supplementary Methods for details. Abbreviations: M, motor, S-A, anterior- somatosensory, S-M, medial-somatosensory, S-BF, somatosensory barrel, S-L, somatosensory-lateral, PT, parietal, A, auditory, V, visual.

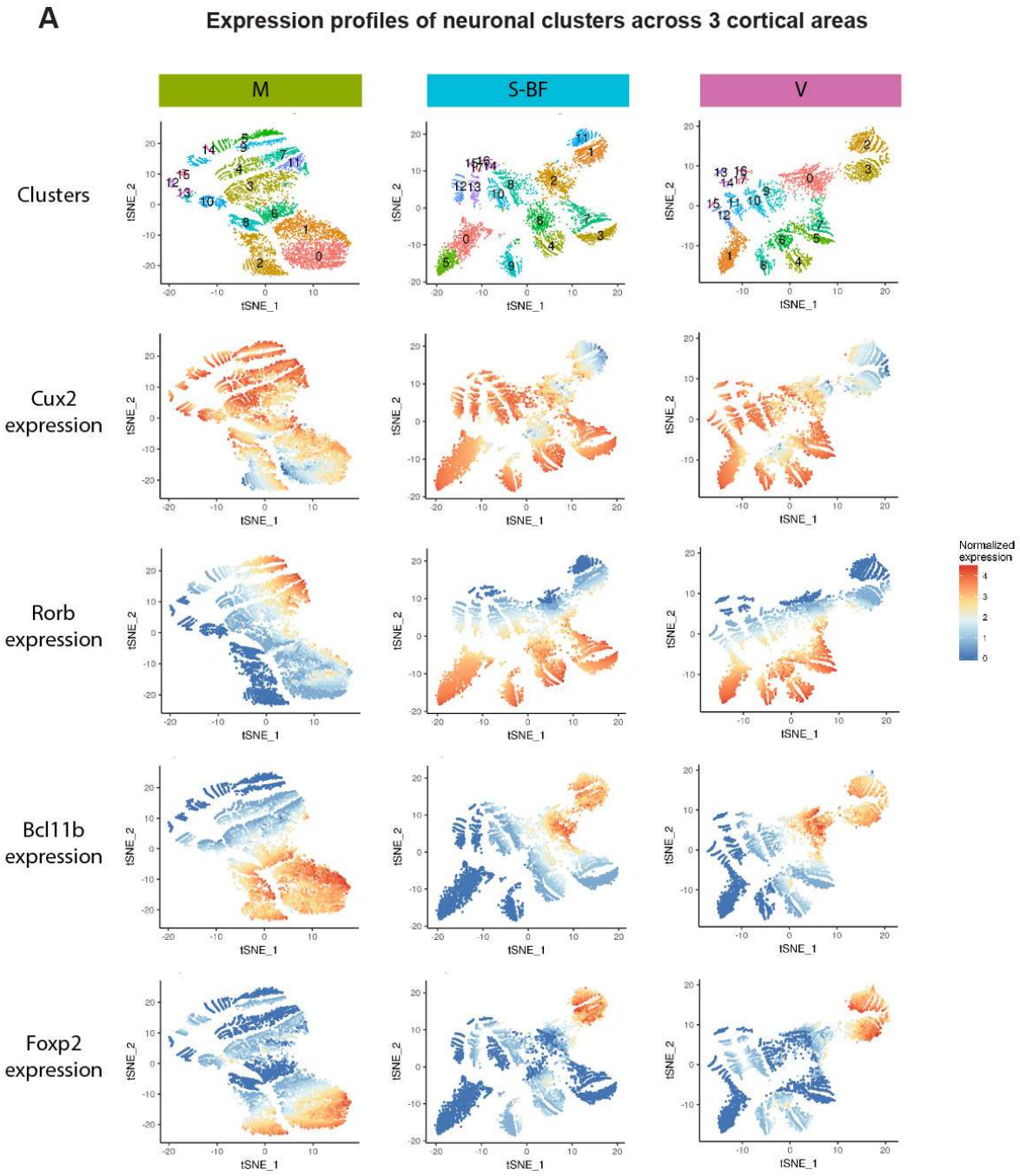

Supplementary Figure 4: Single neuron clusters are distinguished according to layer gene expression patterns.

A) tSNE plots across three different cortical areas (M, motor, S-BF, somatosensory barrel, V, visual) colored according to expression values.

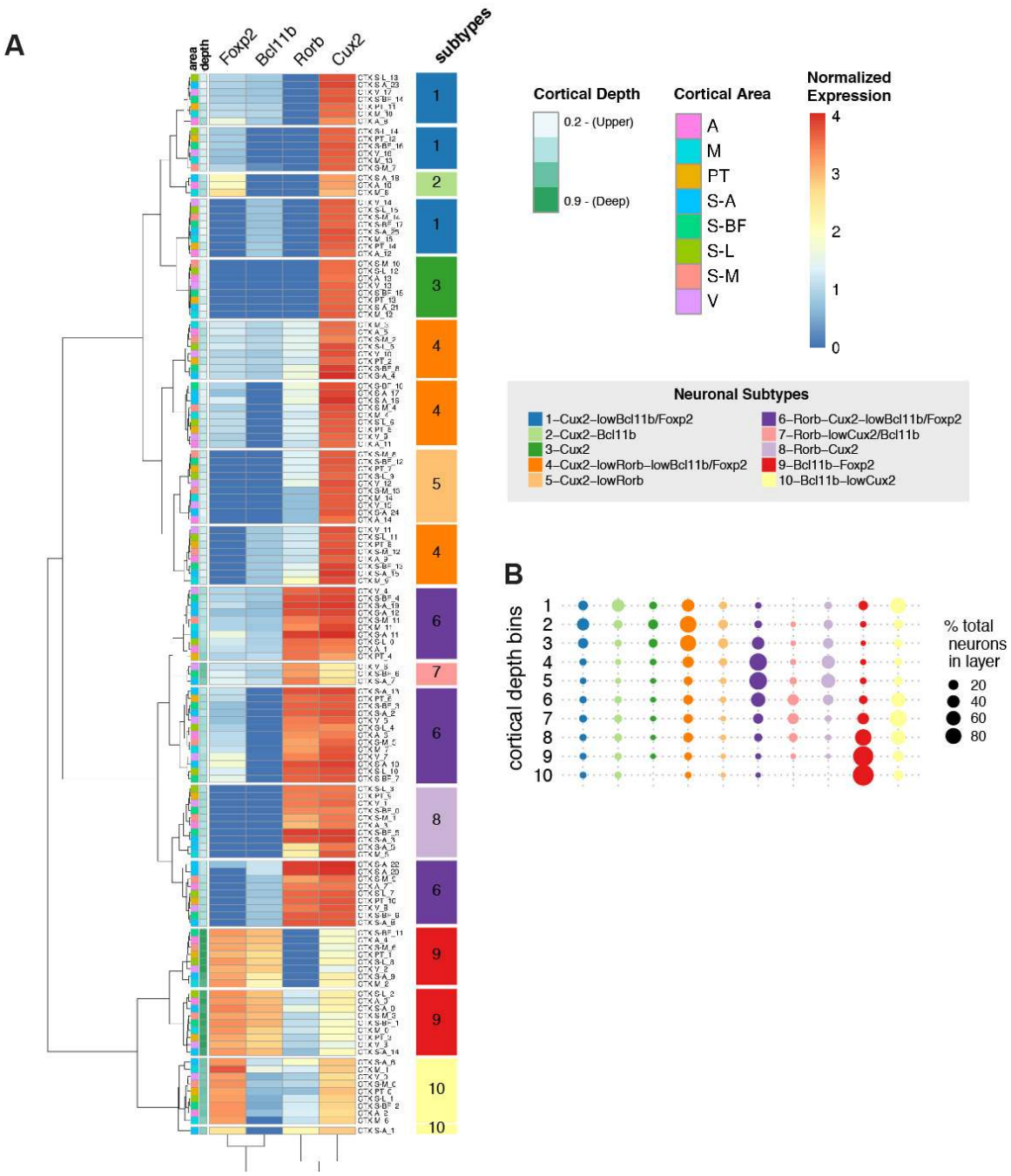

Supplementary Figure 5: Hierarchical clustering distinguishes neuronal subtypes.
A) Hierarchical clustering of clusters from 8 cortical areas (Supplementary Figure 3) according to mean expression profiles of each group. The clustering yielded 18 groups that were manually annotated to 10 major subtypes based on high expression differences and spatial distribution across the cortex. **B**) Neuronal subtypes plotted across 10 cortical depth bins.

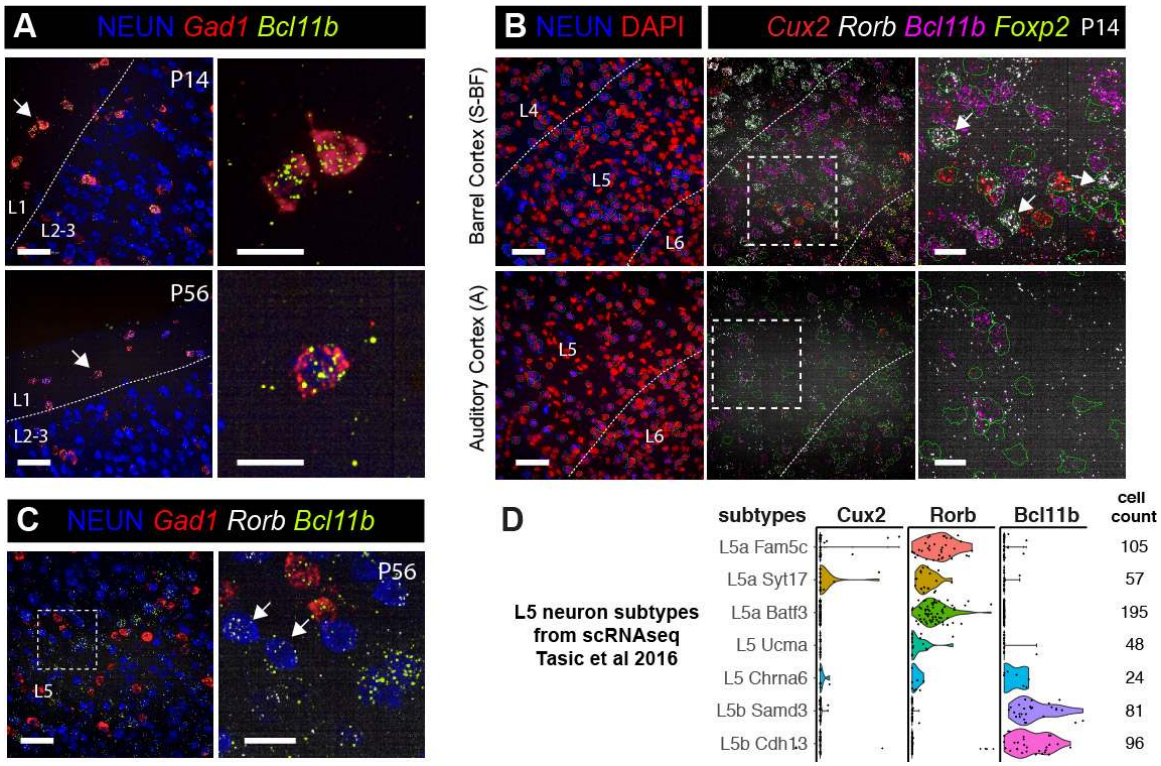

Supplementary Figure 6: smFISH images demonstrating *Cux2*^{mid}*Bcl11b*^{mid}-L1 and *Rorb*^{high}*Bcl11b*^{low}-L5 neuronal populations.

A) Neurons that co-express Cux2 and Bcl11b (cluster #2, arrows) are observed in L1. These interneurons, based on high *Gad1* expression, are present at P14 and are maintained into adulthood at P56. Right panels show higher magnification views of indicated neurons.

B) Area enrichment of novel *Rorb*$^{+}$ L5 subpopulations. *Rorb*^{high}*Cux*^{mid}*Bcl11b*^{low} neurons (cluster #7, arrows) are observed in the L5 of the somatosensory barrel cortex, but are absent from the auditory cortex at P14. The higher magnification view of L5 areas outlined in dashed boxes shown on the right panels.

C) *Rorb*^{high}*Bcl11b*^{low} neurons are maintained into adulthood at P56. *n*=2 mice independently assayed, 3 tissue sections imaged (A-C).

D) Validation of *Rorb*^{high}*Bcl11b*^{low}-L5 subtypes in a published single neuron transcriptomics datasets. Dot plots of single neurons and violin plots showing the segregation of *Rorb* and *Bcl11b* expression amongst molecular subtypes of L5 neurons in the adult visual cortex identified by Tasic et al. Subtypes were named according to the nomenclature in the referenced study. Number of cells observed in each class is shown.

Scalebars: (low magnification panels) 50 μm, (higher magnification panels) 20 μm.

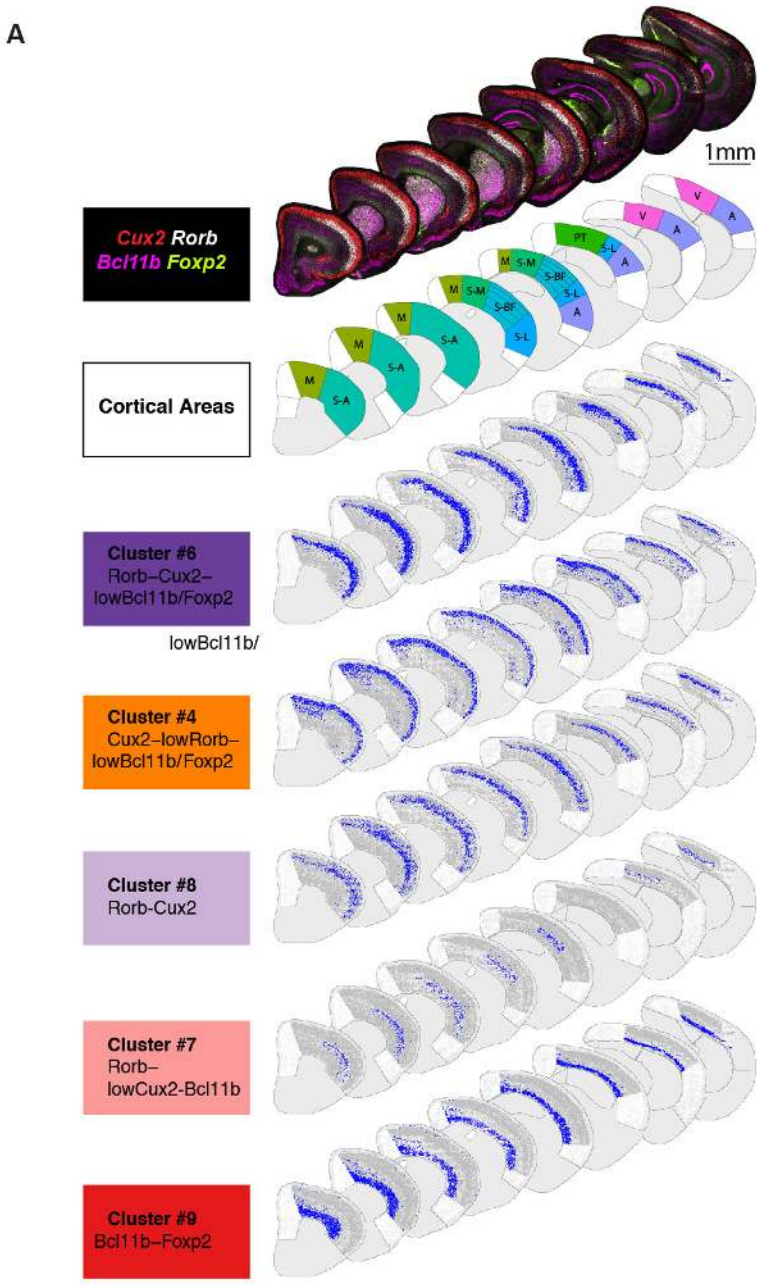

Supplementary Figure 7: Maps showing the single cell level distribution of select neuronal subtypes.

A) (First row) Low magnification images of P14 hemisections from eight select anatomical levels assayed for neuronal layer marker smFISH. (Second row) Maps of broad cortical areas included in neuronal subtype analysis. (Bottom rows) Maps showing the spatial distribution of individual neuronal subtype clusters. *n*=1 mouse, 10 sections independently imaged. Scalebar: 1 mm

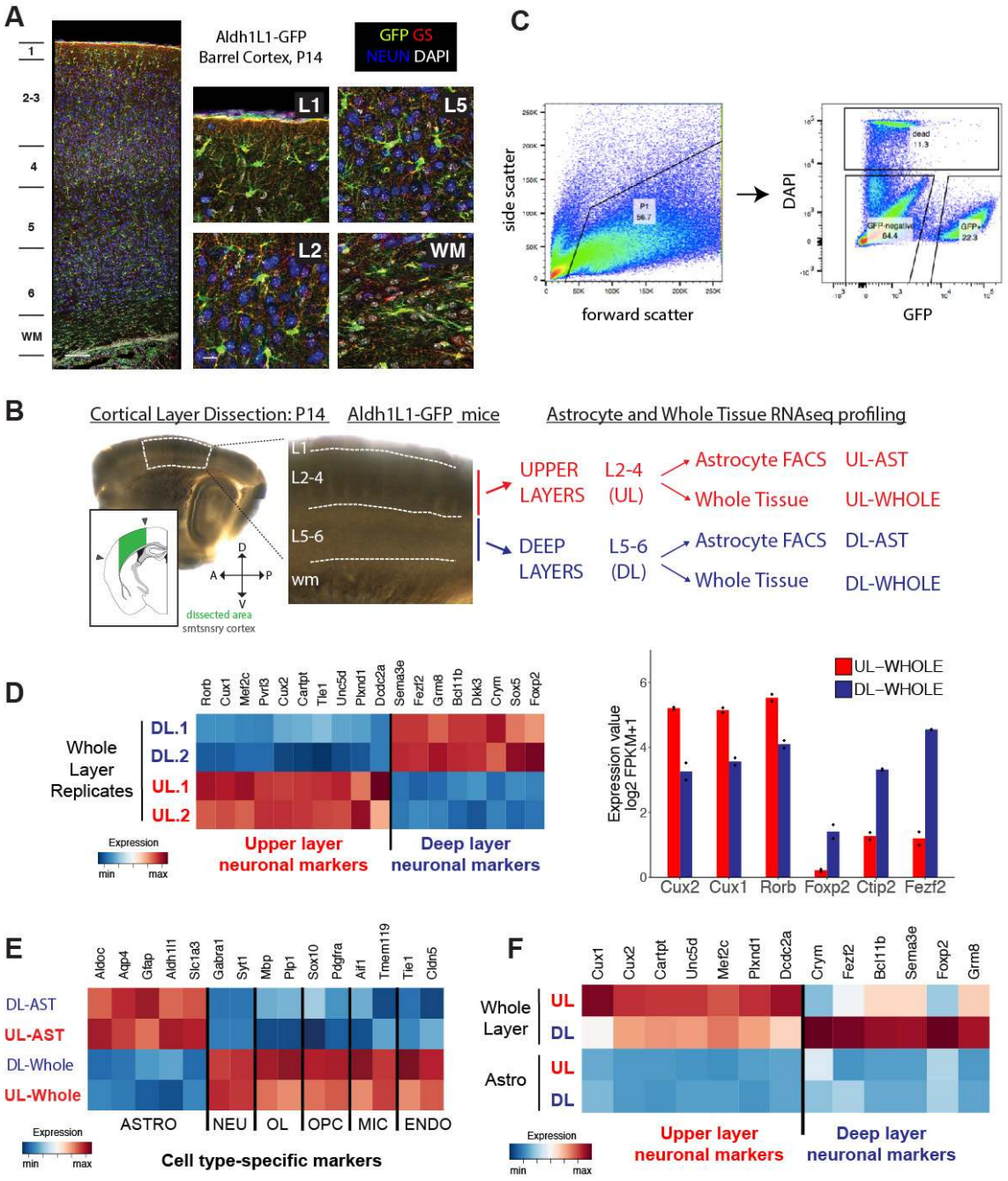

Supplementary Figure 8: Purification and RNAseq expression profiling of upper and deep layer astrocytes.

A) *Aldh11L1-GFP* labeling marks astrocytes across cortical layers and excludes neurons. Confocal images of antibody staining against GFP, NEUN (neuronal marker) and Glutamine Synthetase (GS, astrocyte marker) in the barrel cortex at P14. *Aldh1L1-GFP* labeling marks astrocytes throughout cortical gray matter, white matter and L1-subpia. *n*=2 mice independently assayed, 2 tissue sections imaged.

B) Schematic summarizing layer astrocyte purification and gene expression profiling. (Left) Bright-field images of a sagittal P14 mouse brain slice showing the outline of the layer microdissection in the somatosensory cortex (white dashed lines & also marked green in small

diagram). L4 barrels were used as an anatomical landmark. (Right) FACS-purification and RNAseq profiling strategy.
C) *Aldh1L1-GFP*+ astrocyte isolation by FACS using scatter gates, doublet exclusion (not shown) and sorting for GFP+ cells with dead cell exclusion by DAPI staining.
D) RNAseq expression pattern of known layer neuron markers across whole layer tissue, shown with an expression heatmap and bar-plots, validates the layer microdissection (n=2 biological replicates).
E) Expression pattern of cell type-specific markers confirms the successful purification of astrocytes.
F) The expression of known neuronal layer marker genes does not distinguish layer astrocytes.
Scalebars: (A, large panel) 100 μm, (A, small panels) 25 μm.

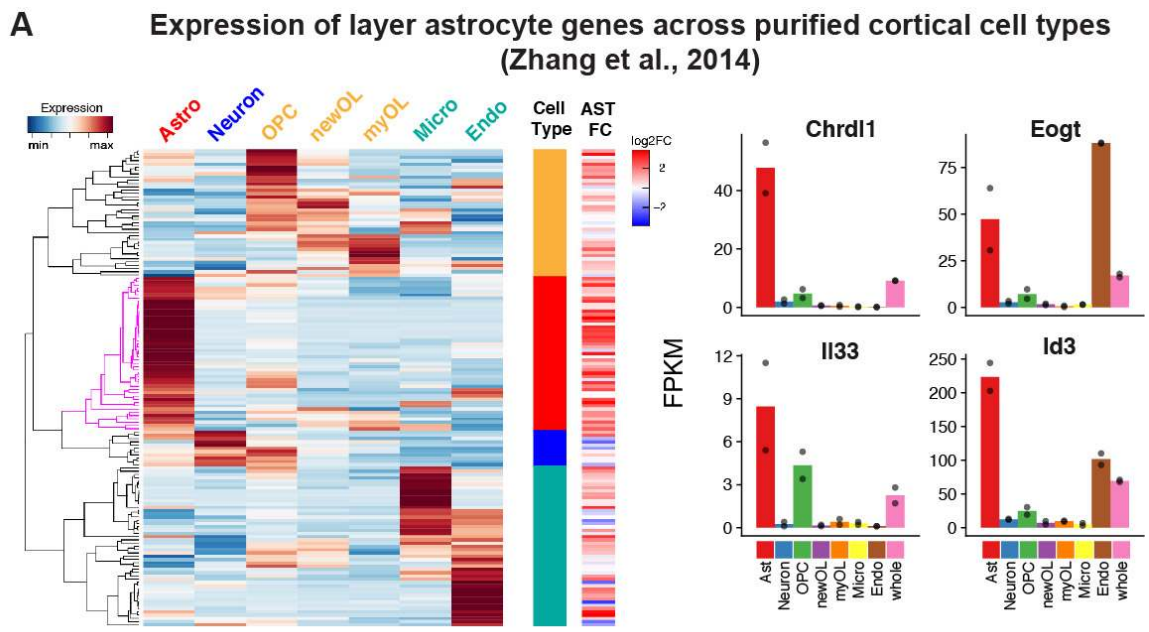

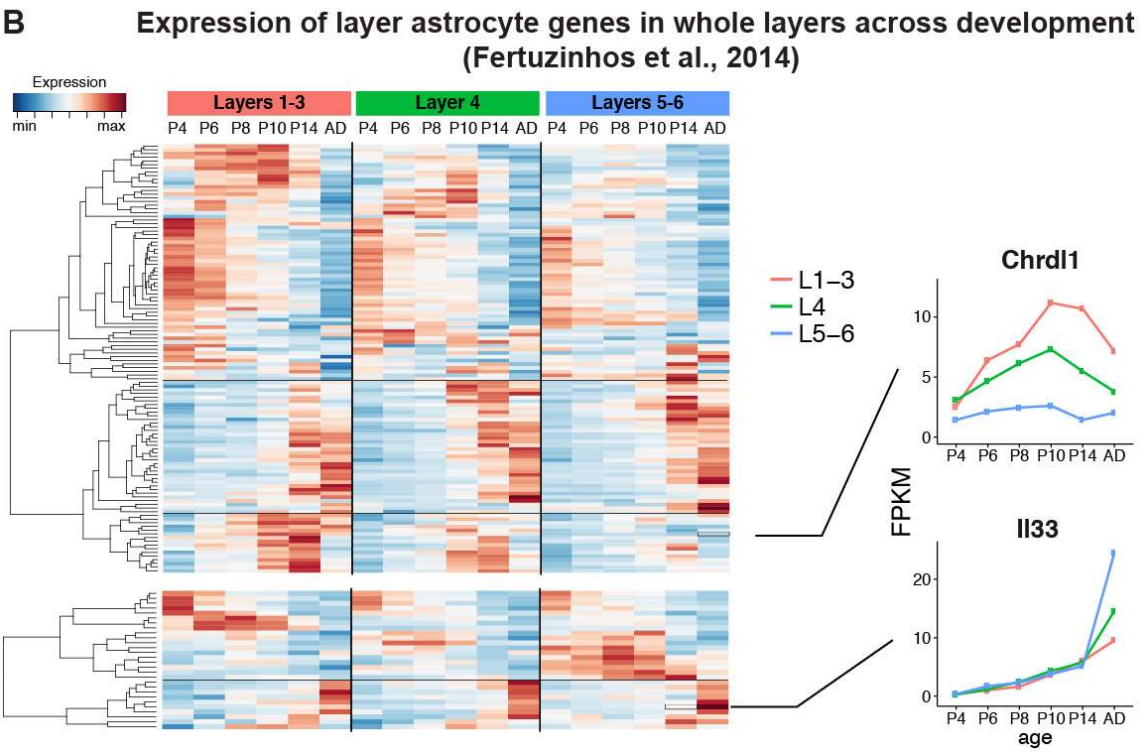

Supplementary Figure 9: Candidate layer astrocyte genes express in laminar and astrocyte-enriched manner across published cortical transcriptome dataset.

A) The expression pattern of 159 genes differentially expressed across upper and deep layer astrocytes across purified cortical cell types. Zhang et al performed RNA-seq analysis of purified mouse cortical astrocytes, neurons, oligodendrocyte precursor cells (OPCs), newly differentiated oligodendrocytes (newOL), myelinating oligodendrocytes (myOL), microglia, and endothelial

cells (Zhang et al., J Neurosci. 2014, *n* =2 biological replciates per cell type). (Left) Heatmap shows that many candidate layer astrocyte genes show expression in astrocytes in Zhang et al's dataset. Many genes have enriched expression in astrocytes, others also express in additional cell types. (Right) Bar plots showing expression of select candidate layer astrocyte genes across cell types. *Chrdl1* expression is highly enriched in astrocytes while *Eogt* and *Id3* also show expression on endothelial cells (validated by smFISH, data not shown).
B) The expression of 163 candidate layer astrocyte genes across whole cortical layer tissue throughout postnatal development and adulthood. Fertuzinhos et al performed RNA-seq analysis manually dissected upper (L1-3), mid (L4) and deep (L5-6) cortical layers at different timepoints during postnatal life and adulthood (Fertuzinhos et al., Cell Rep. 2014). (Left) Heatmap shows that many candidate layer astrocyte genes show laminar and developmentally regulated gene expression in Fertuzinhos et al's dataset. Top heatmap shows upper layer astrocyte enriched genes while the bottom heatmap shows deep layer astrocyte enriched genes. Many genes are upregulated during early postnatal life, consistent with the commencement and progression of cortical astrogenesis after birth (24) (clusters marked in magenta on the dendrogram). (Right) Most layer astrocyte candidate genes show temporally regulated expression throughput postnatal life. *Chrdl1* expression peaks during the second postnatal week yet persists into adulthood. *Il33* expression increases into adulthood.

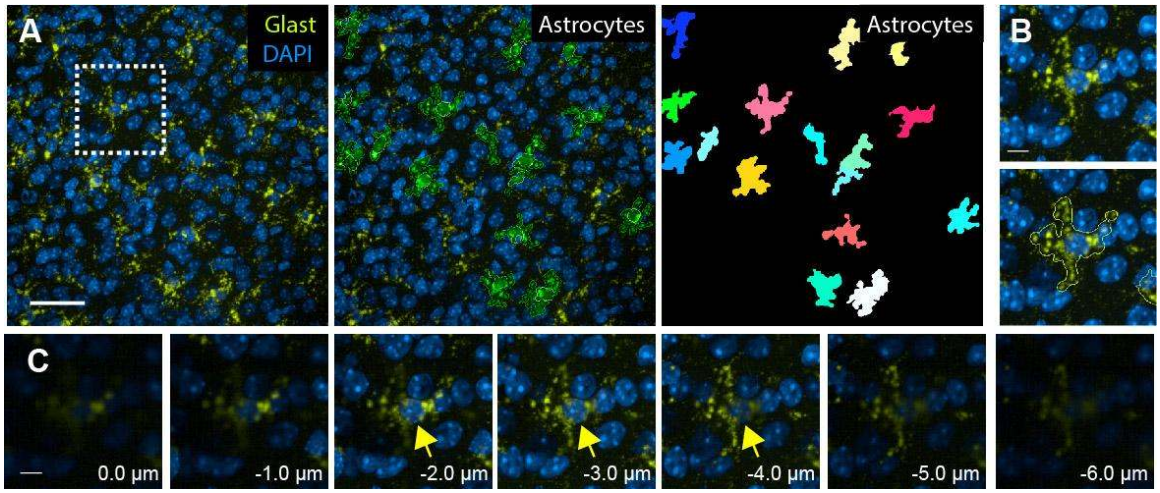

Supplementary Figure 10: Identification of cortical astrocytes with *Glast* smFISH.
A) (Left) Maximum z-projection image showing astrocytes in the P14 barrel cortex upper layers. (Middle) Segmentation of single astrocytes, outlined are astrocyte cell areas (green) and nuclei (white). (Right) Segmentation masks of individual astrocytes.
B) Higher magnification image of an astrocyte indicated with dashed box in A. Bottom panel also shows the outline of the astrocyte cell area in dashed lines.
C) Individual 40X z-planes throughout the same astrocyte. The arrow indicates the astrocyte nuclei marked by Glast and DAPI. For astrocyte segmentation, the z-stack is collapsed into a single plane via a maximum intensity projection. *n*=14 mice assayed across 4 independent batches, 5-10 tissue sections imaged.
Scalebars: (A) 50 µm, (B,C) 10 µm

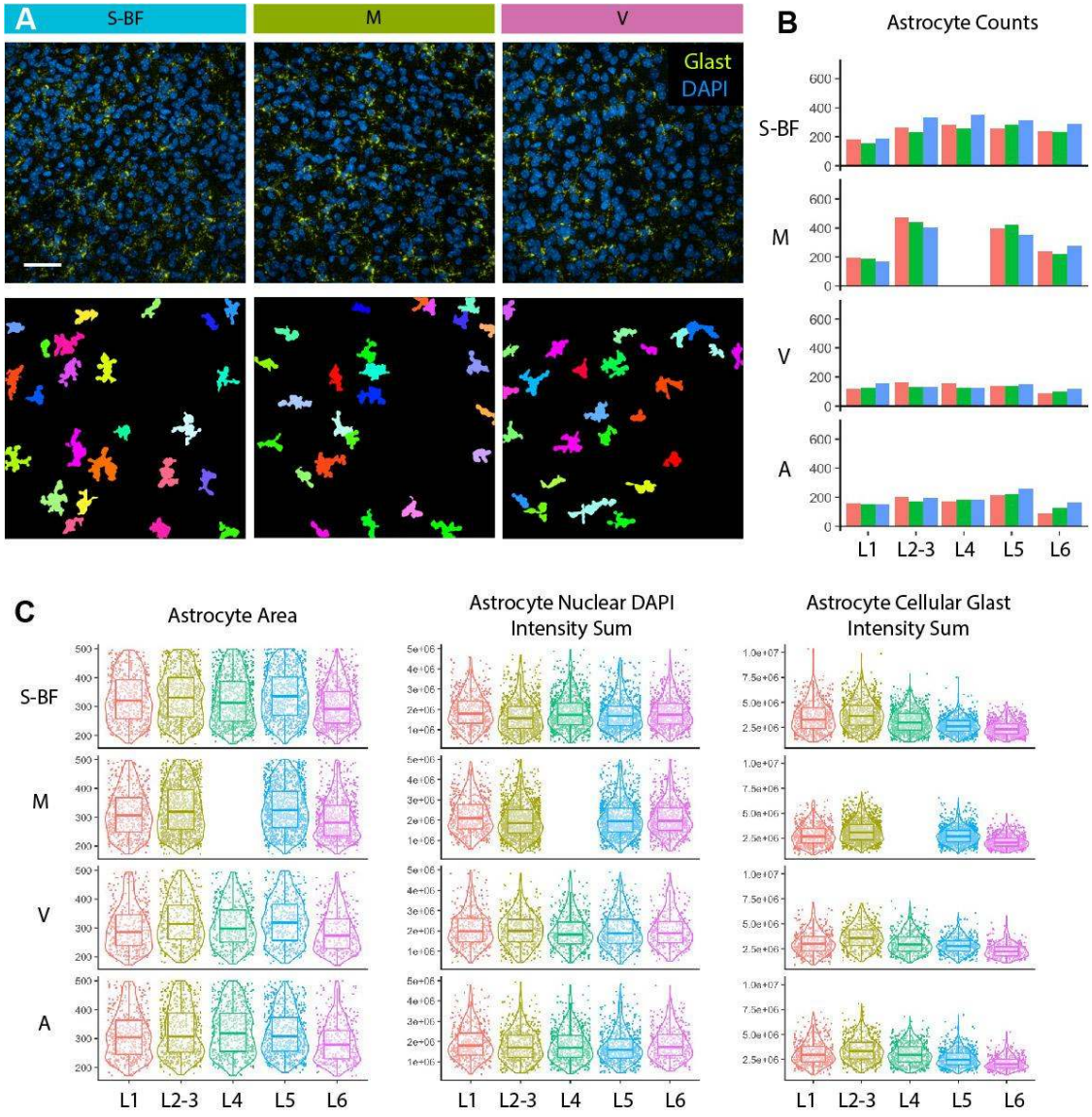

Supplementary Figure 11: Identification of astrocytes across different cortical layers.
A) Images (top) and segmentation masks (bottom) of astrocytes from barrel, motor and visual cortex. Midcortical layers (L4-5) are shown.
B) Astrocyte cell counts across cortical layers and areas are consistent across three technical replicates (different colors).
C) Astrocyte segmentation performs consistently across cortical areas. Violin, box and dot plots showing the cellular features of single astrocytes measured across four cortical areas. Deep layer astrocytes are slightly smaller and show lower expression of Glast than upper layer astrocytes. Number of astrocytes plotted across cortical astrocytes: A: 2628, M: 3777, S-BF: 3878 and V: 1968. *n*=1 mouse, 5-10 tissue sections independently imaged.
Scalebar: (A) 50 µm

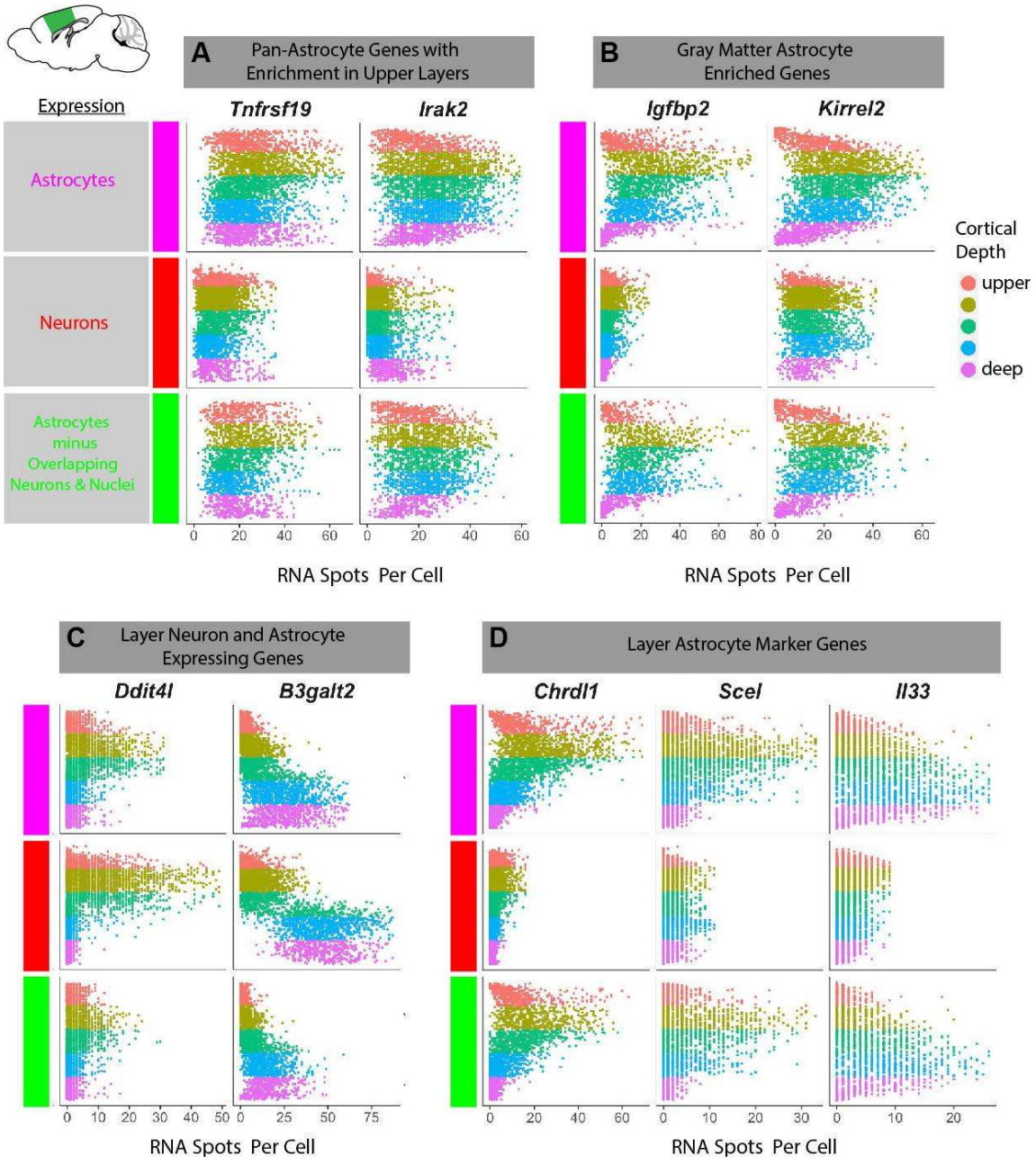

Supplementary Figure 12: Screening and selection of top layer astrocyte markers. Quantification of single astrocyte, neuron and filtered astrocyte (i.e. removal of z-overlapping neurons and non-astrocyte nuclei) in situ expression of candidate layer astrocyte genes identifies several spatial and cell type-specific expression patterns. Screened genes show pan-astrocyte (A), gray matter astrocyte (B), astrocyte and neuron (C), and layer astrocyte enriched (D) expression patterns. *n*=2 mice assayed independently, 3 tissue sections imaged per replicate.

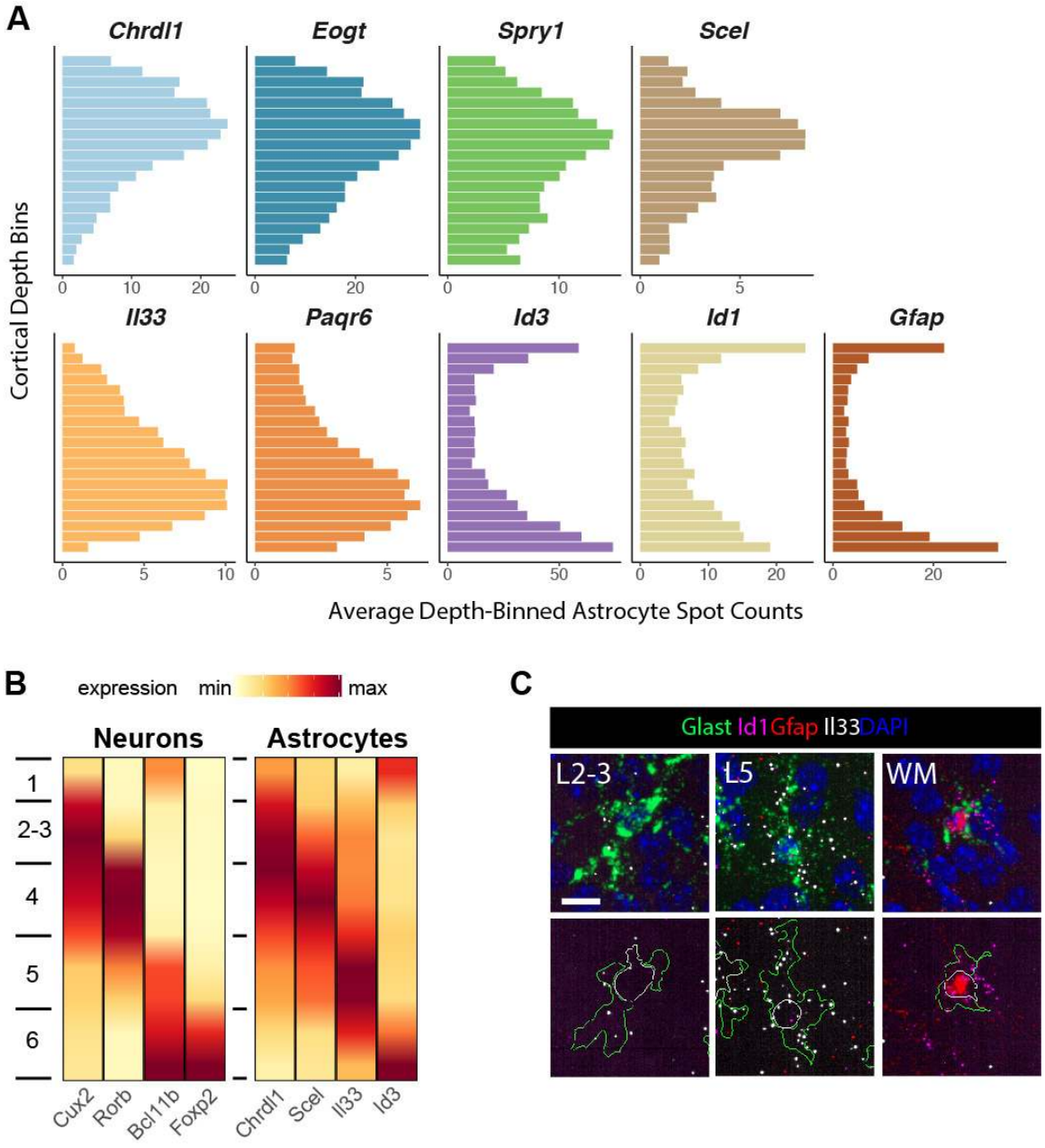

Supplementary Figure 13: Astrocyte layer gene expression diverges from neuronal laminae.
A) Quantification of astrocyte layer marker expression across cortical depth. Plots show the single astrocyte expression averaged across ten cortical depth bins in the P14 somatosensory cortex (n=2 pooled biological replicates).
B) Interpolated tile expression plots comparing neuron vs astrocyte layer marker expression across cortical depth in the P14 barrel cortex (n=3 pooled tissue sections across the somatosensory cortex from one biological replicate). Astrocyte layer expression domains diverge from sharply refined neuronal laminae. A Chi2-test comparing the expression of astrocyte to neuron layer markers cortical depth supported this conclusion (p-value < 1e-16).
C) *Il33* expression is enriched in L5 astrocytes but absent from white matter astrocytes at P14. *n*=2 mice independently assayed, 3 tissue sections imaged.
Scalebar: (C) 10 μm

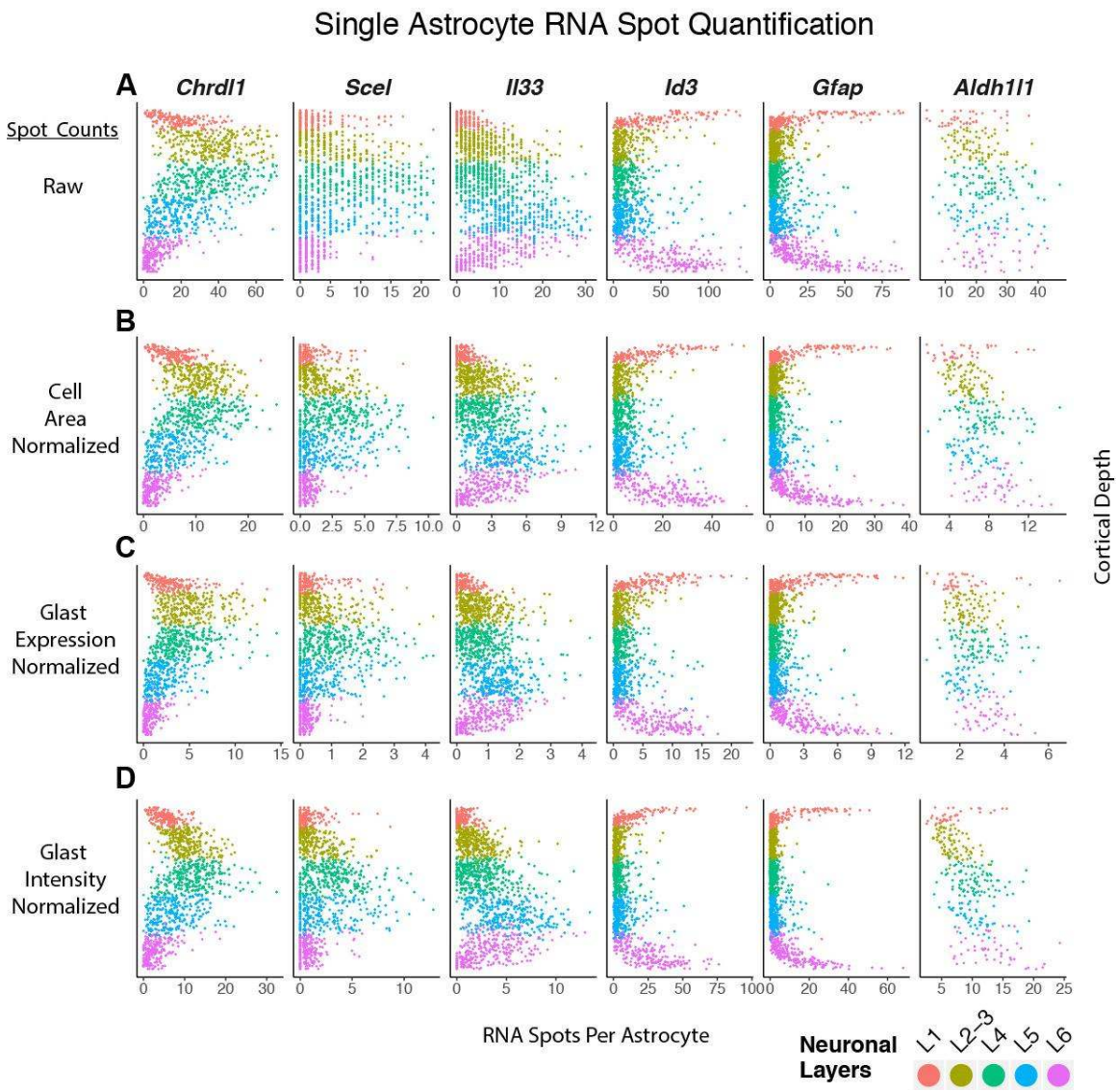

Supplementary Figure 14: The observed astrocyte layer gene expression patterns are not artifacts of cell size or *Glast* expression level differences.
Quantification of single astrocyte expression across cortical depth in the P14 barrel cortex (n=3 pooled tissue sections from one biological replicate). The expression of identified layer astrocyte markers, the white matter astrocyte marker *Gfap* and the pan-astrocyte marker *Aldh1l1* are plotted as single cell RNA spot counts that are (A) raw, or normalized to (B) astrocyte area, (C) single cell *Glast* spot counts, and (D) single cell *Glast* signal intensity. *n*=2 mice independently assayed, 3 tissue sections imaged.

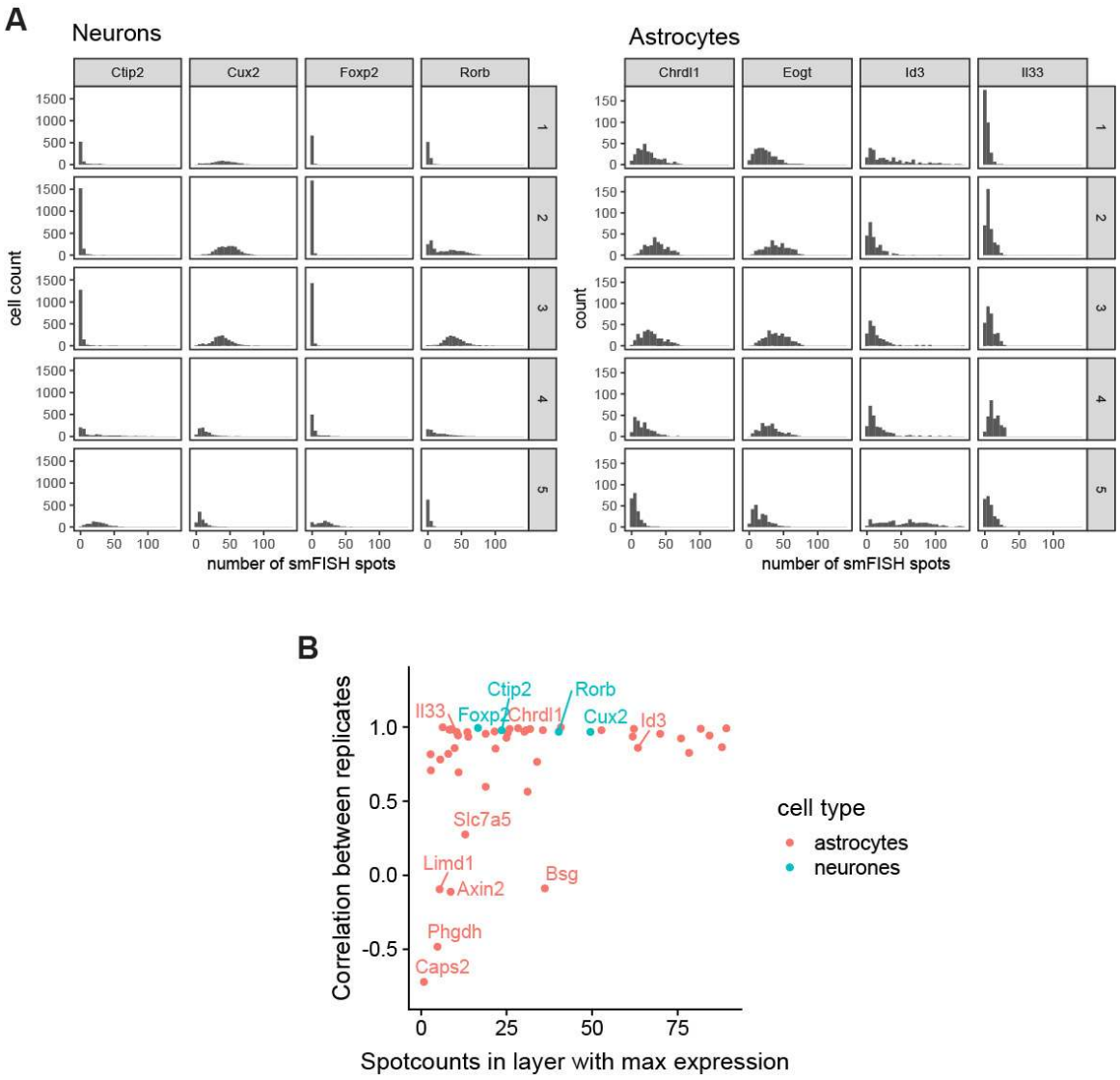

Supplementary Figure 15: Reproducibility of astrocyte expression patterns across gene expression levels.

A) The best neuronal (left) and astrocyte (right) cortical layer markers have similar expression level in bins with highest expression. Comparison of expression level (X-axis) histogram counts (Y-axis) of neuronal and astrocyte cortical layer markers (columns) across 5 spatial bins (rows).

B) Spatial profiles of most astrocyte and neuron layer markers (color) correlate well between biological replicates (Y-axis) regardless of the expression level (X-axis, expression level in bins where genes are maximally expressed). Selected best markers as well as the genes with the least reproducible patterns are marked. Multiple tissue sections across the somatosensory cortex were assayed from two P14 mice for the analysis.

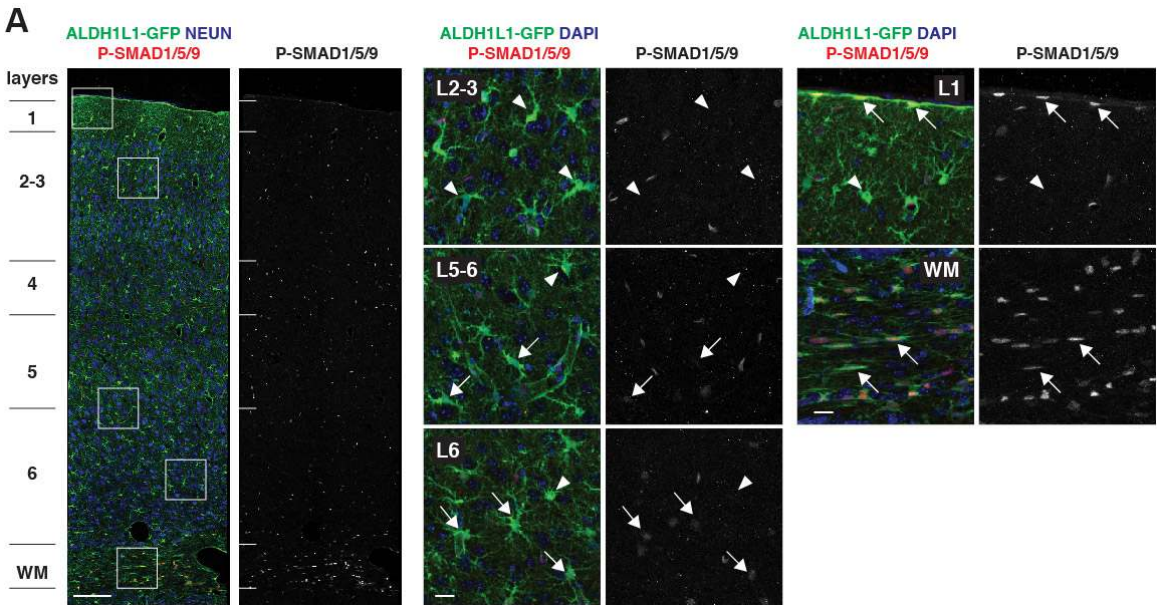

Supplementary Figure 16: Layer 6 astrocyte enriched Id3 expression is consistent with activated BMP signaling in this population assessed pSmad immunohistochemistry.

A) L6, WM and L1-subpia astrocytes show higher levels of phosphorylated Smad (pSmad) immunostaining that indicates Id protein activity. This pattern is consistent with the expression pattern of *Id3* mRNA detected with LaSTmap smFISH. Images from the P14 somatosensory cortex of the Aldh1L1-GFP astrocyte reported mice are shown. Arrows indicate astrocytes with high pSmad, while arrowheads indicate astrocytes with low pSmad staining. *n*=2 mice assayed in one experiment, 3 tissue sections imaged. b Scalebar: (large panels) 100 μm, (small panels) 25 μm.

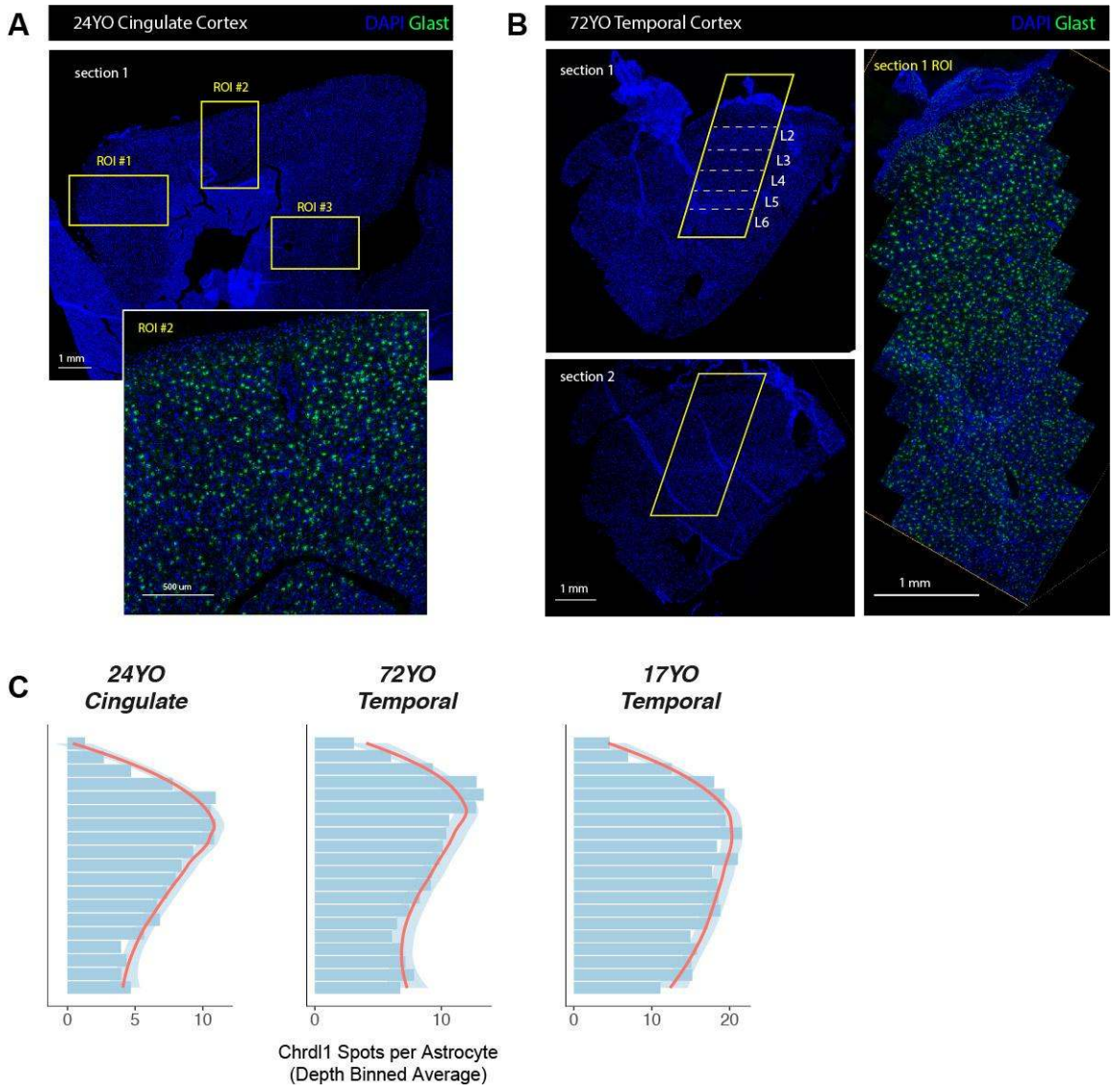

Supplementary Figure 17: *Chrdl1* expression is enriched in upper layer astrocytes in the adult human cortex.

A) Astrocytes in the 24 year old cingulate cortex. Low magnification images show DAPI staining of a section through the cingulate cortex (top) and Glast smFISH of the ROI #2 (bottom). Boxed regions of interest were imaged at 40X to quantify layer astrocyte expression of *Chrdl1*.

B) Astrocytes in the 72 year old temporal cortex. Low magnification images show DAPI staining of two sections through the temporal cortex (left) and Glast smFISH of the ROI on the first section (right). Boxed regions of interest were imaged at 40X to quantify layer astrocyte expression of *Chrdl1*.

C) Quantification of depth binned average single astrocyte expression of Chrdl1 across the 24YO cingulate, 72YO temporal and 17YO temporal cortex samples. The three samples were assayed and imaged independently.

Scalebars: (DAPI) 1 mm, (DAPI-*Glast*) 0.5 mm

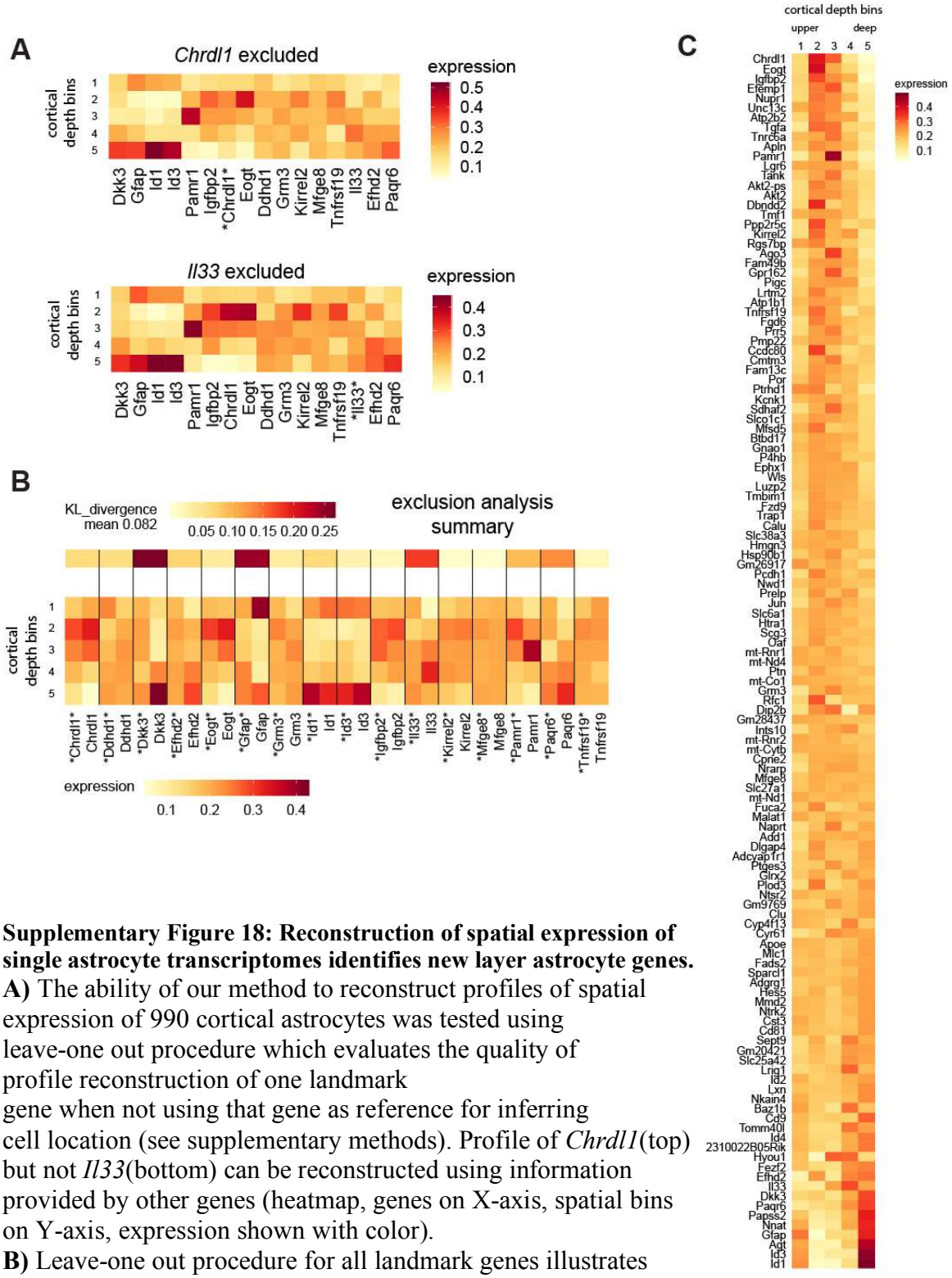

Supplementary Figure 18: Reconstruction of spatial expression of single astrocyte transcriptomes identifies new layer astrocyte genes. **A)** The ability of our method to reconstruct profiles of spatial expression of 990 cortical astrocytes was tested using leave-one out procedure which evaluates the quality of profile reconstruction of one landmark gene when not using that gene as reference for inferring cell location (see supplementary methods). Profile of *Chrdl1*(top) but not *Il33*(bottom) can be reconstructed using information provided by other genes (heatmap, genes on X-axis, spatial bins on Y-axis, expression shown with color). **B)** Leave-one out procedure for all landmark genes illustrates which genes have profiles that are easily reconstructed (marked with asterisk) according to visual inspection, and relative entropy (top bar) compared to observed profile. **C)** Expression profiles (color) of 125 significantly layer-restricted genes (Y-axis) across 5 spatial bins (X-axis).

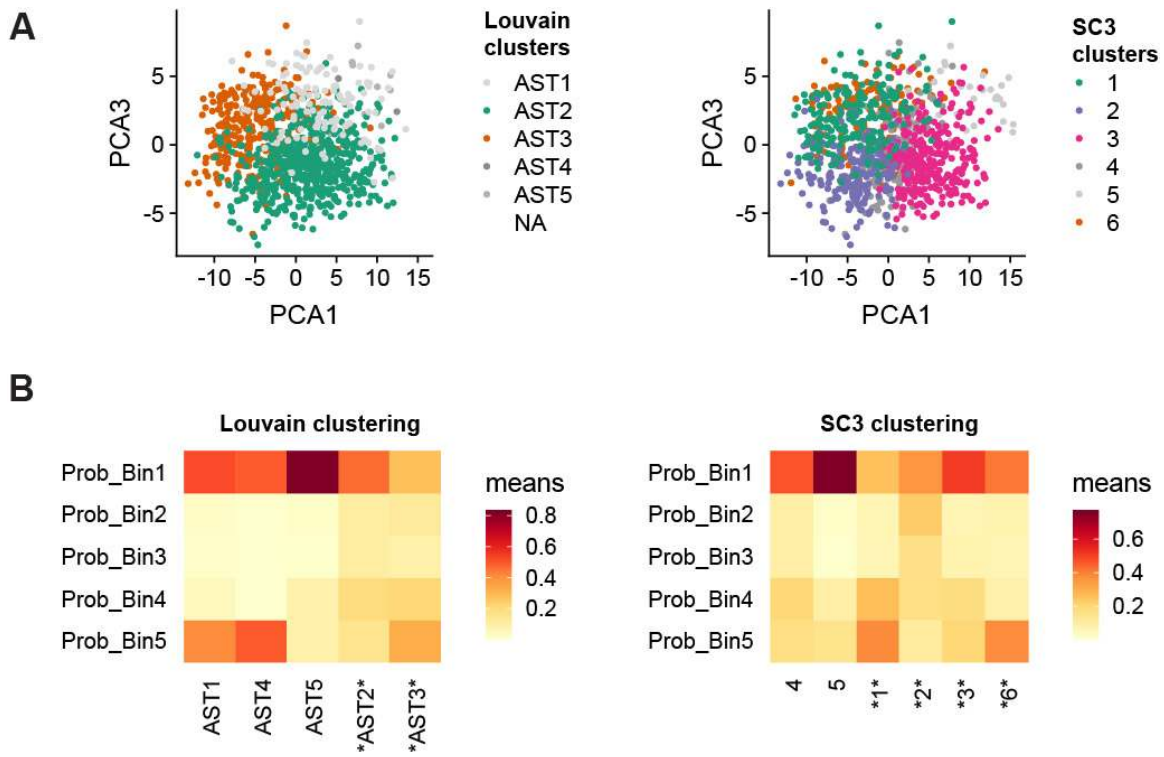

Supplementary Figure 19: scRNA-seq subtypes identified with unsupervised clustering do not show distinct pattern of layer locations

A) Louvain (left) and SC3 (right) unsupervised clustering methods identify cortical astrocyte subtypes (color), shown in Principal Component dimensions (PC1 – X-axis, PC2 – Y-axis) from 990 profiled cells. Louvain clustering is obtained from Batiuk et al (23) where cluster AST2 and AST3 are cortical astrocytes. SC3 clustering was performed cortical subset of the data using default parameters. The number of clusters was chosen based on p-value for the clustering and presence of coherent markers for most clusters. Clusters 4 and 5 were considered as poor quality due to the lack of markers and that these are hypothalamic clusters with few cells in the cortex.

B) Clusters have overall similar location and cells from most clusters are located in bin 1 and 5 (corresponding to layer 1 and 6). Probability of cell assignment (color) to spatial bins (Y-axis) average across cells from the same cluster (X-axis). High-quality Louvain (left) and SC3 (right) clusters are marked with asterisk. SC3 cluster 1 and 2 have higher location probability in middle layers than AST2 and 3, however, both cells from both Louvain and SC3 clusters do not follow clear layer pattern.

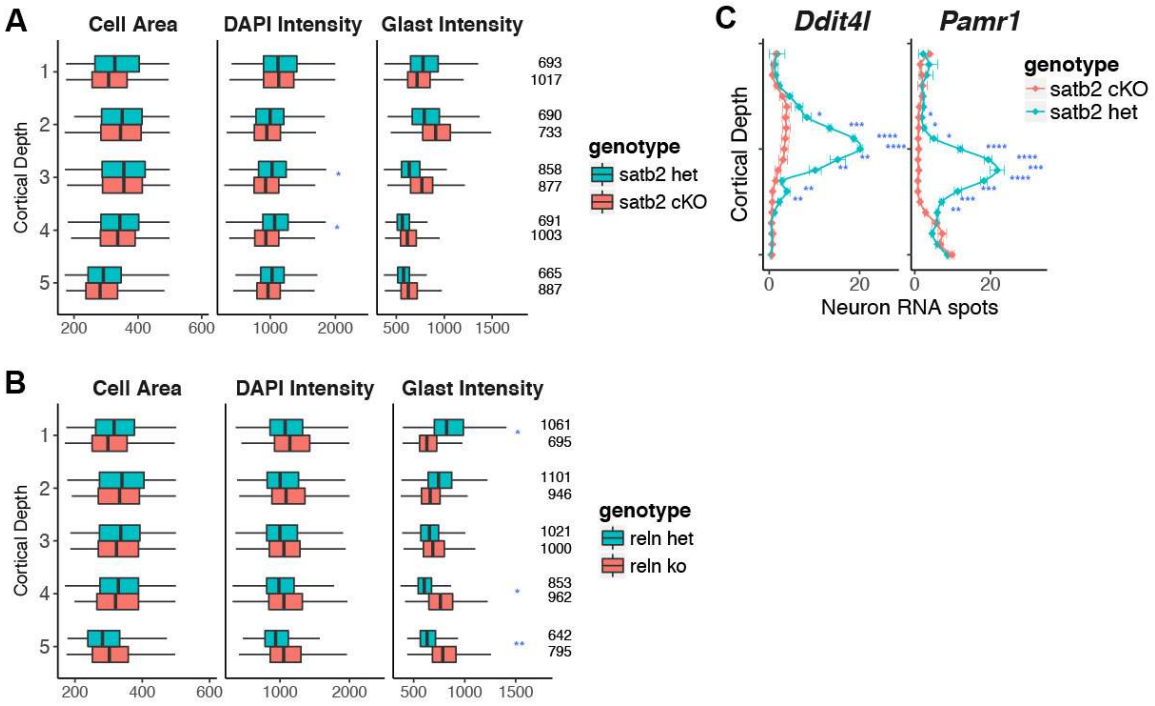

Supplementary Figure 20: Astrocyte cellular phenotypes in neuronal layer switch experiments and loss of L4 neuron gene expression in *Satb2* cKO.
A) Boxplots comparing astrocyte area, DAPI and Glast intensity between *Satb2* cKO and littermate controls in the P14 barrel cortex. No significant change is observed in these astrocyte features upon *Satb2* cKO. Cell counts per genotype per cortical depth bin are shown on the right (n=3 pooled biological replicates per genotype).
B) Boxplots comparing astrocyte area, DAPI and Glast intensity between *Reeler* and littermate controls in the P14 barrel cortex. In *Reeler*, the difference in *Glast* expression between superficial and deep astrocytes is inversed, consistent with the inversion of astrocyte layers based on marker gene expression. Cell counts per genotype per cortical depth bin are shown on the right (n=3 pooled biological replicates per genotype).
C) Quantification of cortical depth binned neuronal layer marker expression in cKO vs control (n=3 pooled biological replicates per genotype). *Satb2* cKO shows loss of L4 neuron gene expression based on additional L4 markers, *Ddit4l* and *Pamr1*.
Two-tailed student's t-test was used. Data represent mean ± s.d. *P < 0.05,**P < 0.01, ***P < 0.001.

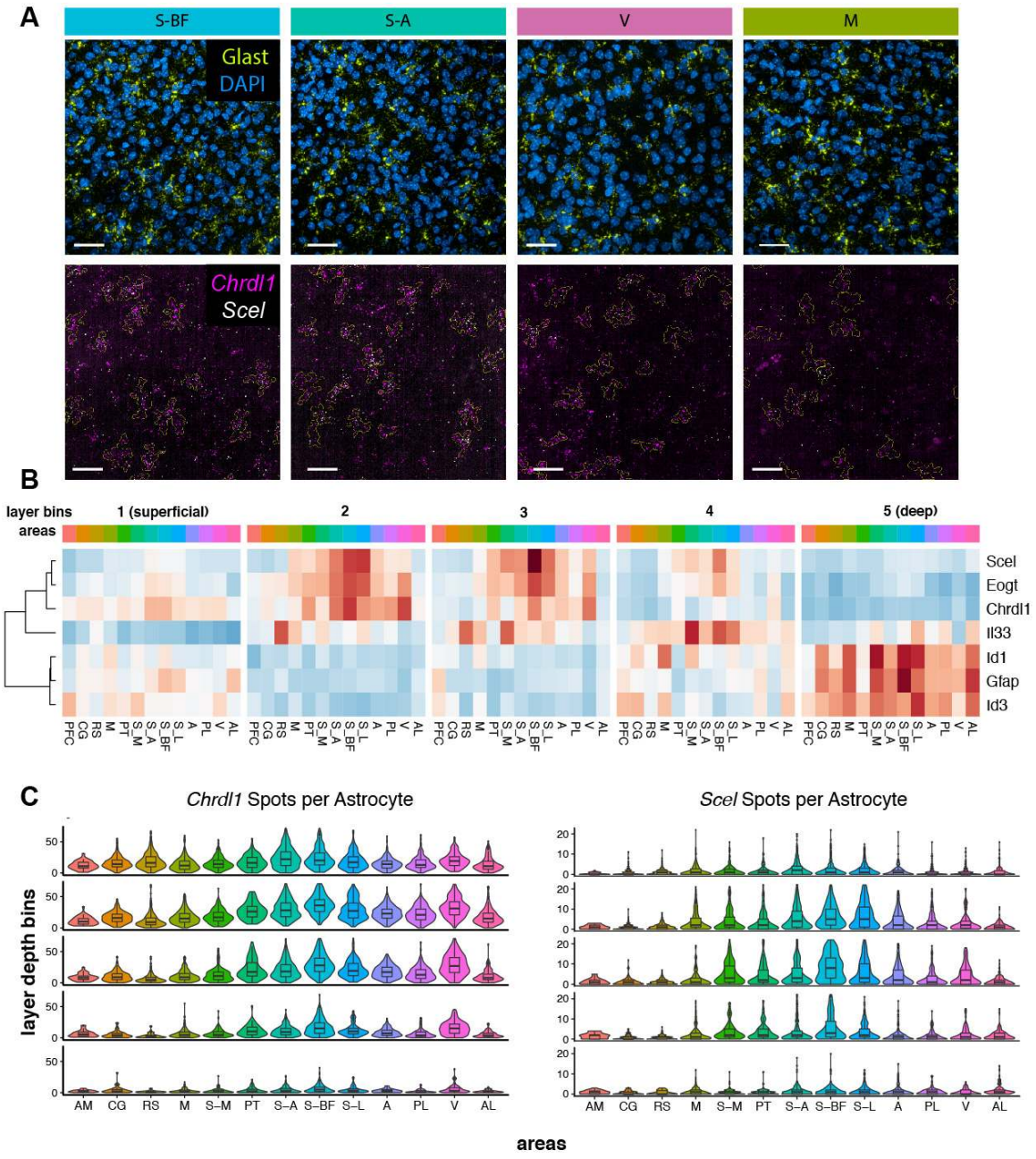

Supplementary Figure 21: Astrocyte layer gene expression varies across cortical areas.
A) Images showing the enrichment of *Scel* and *Chrdl1* expression in somatosensory areas over motor and visual cortex. In the bottom panels, the single astrocyte segmentations are shown in green.
B) Expression heatmap showing the expression of layer astrocyte markers across cortical depth and areas (assayed over n=10 tissue sections from one biological replicate).
C) Violin plots showing the quantification of single astrocyte expression of *Chrdl1* and *Scel* across cortical layers and areas. Number of cells across cortical areas: AM: 141, CG: 858, RS: 1276, M: 1298, S-M: 745, PT: 393, S-A: 2472, S-BF: 1231, S-L: 897, A: 838, PL: 690, V: 668 and AL: 686. *n*=1 mouse, 10 tissue sections independently imaged.
Scalebar: 50 µm

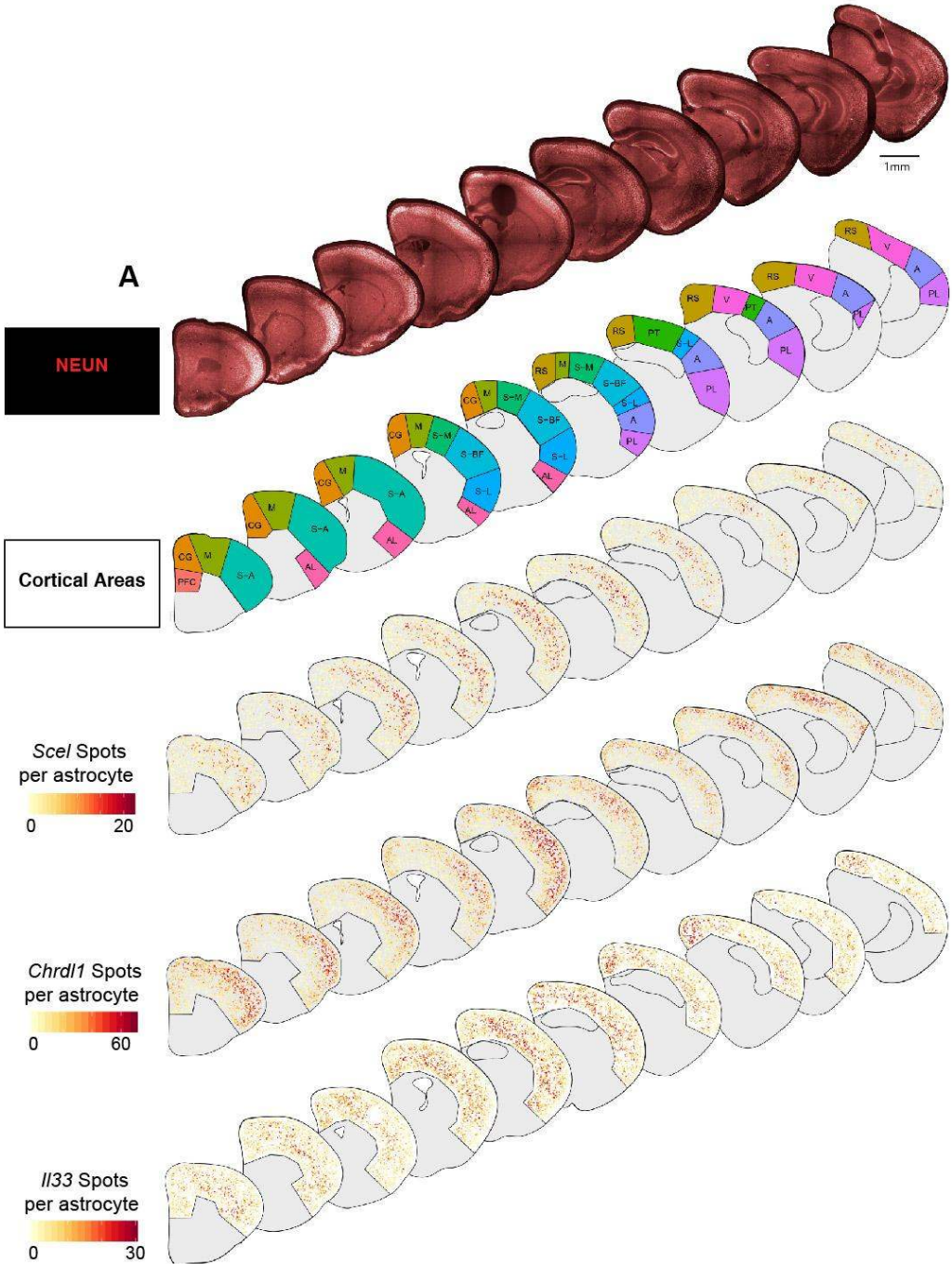

Supplementary Figure 22: Maps showing the single cell level distribution of select neuronal subtypes.

A) (First row) Low magnification images of P14 hemisections from ten anatomical levels assayed for NEUN IHC. (Second row) Maps of broad cortical areas included in analysis of regional astrocyte gene expression. (Bottom rows) Maps showing single astrocyte expression of *Scel*, *Chrdl1* and *Il33* across the cortex. *n*=1 mouse, 10 tissue sections independently imaged. Scalebar: 1 mm

Supplementary Table Legends

Supplementary Table 1: Single cortical neuron smFISH dataset. Table listing cellular, anatomical and gene expression measurements of 69,318 single neurons identified across the P14 cortex. The cluster assignments of 46,887 single neurons used for subtype identification across 8 broad cortical areas are also listed. Every row is a single neuron and the table columns are described in the "Supp Table 1 Metadata" sheet.

Supplementary Table 2: Single cortical astrocyte smFISH screen dataset. Table listing cellular, anatomical and gene expression measurements of 41,187 single astrocytes screened in the somatosensory cortex across two biological replicates. 46 candidate layer astrocyte markers as well as the pan-astrocyte marker *Aldh1l1* and the white matter astrocyte marker *Gfap* were multiplexed with the astrocyte marker *Glast* across multiple slides, these are listed under "Supp Table 2 Metadata". Every row is a single astrocyte and the table columns are described in the metadata sheet.

Supplementary Table 3: RNAscope probes used in this study. Table listing all of the RNAScope probes, their mRNA target regions and ACD catalog numbers.

Supplementary Table 4: Automated histology protocols and reagents. Tables listing the automated 4-plex RNAScope smFISH and IHC protocol used on the Leica BOND RX and the consumable reagents.

Supplementary Table 5: Imaging settings. Tables listing the fluorophores, light sources, exposure times and emission filters used for mouse and human tissue imaging.

Supplementary Table 6: The single neuron segmentation and gene expression quantification pipeline. Table listing all of the steps and settings used in the Harmony software.

Supplementary Table 7: The single astrocyte segmentation and gene expression quantification pipeline. Table listing all of the steps and settings used in the Harmony software.

Supplementary Table 8: List of abbreviations for cortical areas. Table listing all the broad cortical areas examined in this study.

Supplementary Table 9: Cortical layer astrocyte RNAseq data. The RNAseq expression pattern and differential gene expression statistics of 159 candidate layer astrocyte markers. The list of 46 top genes screened with smFISH is also provided. The table columns are described in the "Supp Table 9 Metadata" sheet.

Supplementary Table 10: Reconstruction of spatial expression– layer assignment probability of cells. The matrix of posterior probability of cell assignment which shows the probability of each cell belonging to each spatial bin (see methods equation 6).

Supplementary Table 11: Reconstruction of spatial expression – average profiles of later-restricted genes. The table shows average reconstructed expression levels for 4963 genes that are detected in at least 145 scRNA-seq cells, including Kruskal–Wallis test p-value and q-value corrected with q value method.